Simple Spectral Models for Atmospheric Radiative Cooling

NADIR JEEVANJEE[a] AND STEPHAN FUEGLISTALER

Department of Geosciences, Princeton University, Princeton, New Jersey

(Manuscript received 28 November 2018, in final form 2 December 2019)

ABSTRACT

Atmospheric radiative cooling is a fundamental aspect of Earth's greenhouse effect, and is intrinsically connected to atmospheric motions. At the same time, basic aspects of longwave radiative cooling, such as its characteristic value of 2 K day^{-1}, its sharp decline (or "kink") in the upper troposphere, and the large values of CO_2 cooling in the stratosphere, are difficult to understand intuitively or estimate with pencil and paper. Here we pursue such understanding by building simple spectral (rather than gray) models for clear-sky radiative cooling. We construct these models by combining the cooling-to-space approximation with simplified greenhouse gas spectroscopy and analytical expressions for optical depth, and we validate these simple models with line-by-line calculations. We find that cooling rates can be expressed as a product of the Planck function, a vertical emissivity gradient, and a characteristic spectral width derived from our simplified spectroscopy. This expression allows for a pencil-and-paper estimate of the 2 K day^{-1} tropospheric cooling rate, as well as an explanation of enhanced CO_2 cooling rates in the stratosphere. We also link the upper-tropospheric kink in radiative cooling to the distribution of H_2O absorption coefficients, and from this derive an analytical expression for the kink temperature $T_{\text{kink}} \approx$ 220 K. A further, ancillary result is that gray models fail to reproduce basic features of atmospheric radiative cooling.

1. Introduction

Atmospheric radiative cooling is a fundamental aspect of Earth's greenhouse effect, and is intrinsically connected to atmospheric motions. Although radiative equilibrium states with no atmospheric cooling are possible in principle, on Earth such states are unstable; this leads to a turbulent troposphere with deep convection in the tropics and baroclinic eddies in midlatitudes, both of which lead to non-radiative-equilibrium temperature profiles, which exhibit radiative cooling.

This tight coupling between radiative cooling, turbulence, and the hydrological cycle has many consequences. Perhaps foremost, radiative cooling characterizes the large-scale circulation by governing the clear-sky subsidence velocity (e.g., Mapes 2001). In particular, the clear-sky subsidence velocity turns out to be remarkably uniform across the globe, because radiative cooling is; indeed, a latitude–height distribution of the clear-sky, longwave only heating $\mathscr{H}$ (Fig. 1a, taken from ECMWF reanalysis) shows that throughout most of the troposphere, $\mathscr{H} = -2 \pm 0.5$ K day^{-1}. Despite the robustness of this value, however, we currently lack the tools to estimate $\mathscr{H}$ from first principles:[1] gray models are insufficient for this task (as discussed below), leaving only numerical radiative transfer schemes as a means for calculating $\mathscr{H}$.

Another consequence of the coupling between radiative cooling and turbulence is that wherever radiative cooling declines in the upper troposphere, latent heating by convection and baroclinic eddies must follow suit. To get a feel for this, we collapse the ECMWF cooling distribution in Fig. 1a onto a global radiative cooling

[a] Current affiliation: Program in Atmosphere and Ocean Sciences, Princeton University, Princeton, New Jersey.

Corresponding author: Nadir Jeevanjee, nadirj@princeton.edu

[1] Given the average outgoing longwave radiation (OLR) of 240 W m^{-2} and a tropospheric mass of ~8000 kg m^{-2}, one can estimate a global *average* $\mathscr{H}$ as $\mathscr{H} \approx -(240\ \text{W m}^{-2})/(8 \times 10^3\ \text{kg m}^{-2} \times 1000\ \text{J kg}^{-1}\ \text{K}) = -2.5 \times 10^{-5}$ K s^{-1} $= -2.5$ K day^{-1}. This calculation cannot tell us about the vertical distribution of $\mathscr{H}$, however, and moreover assumes that all OLR emanates from the atmosphere (rather than the surface), an assumption that is reasonable in the global mean but does not hold locally (Costa and Shine 2012).

DOI: 10.1175/JAS-D-18-0347.1

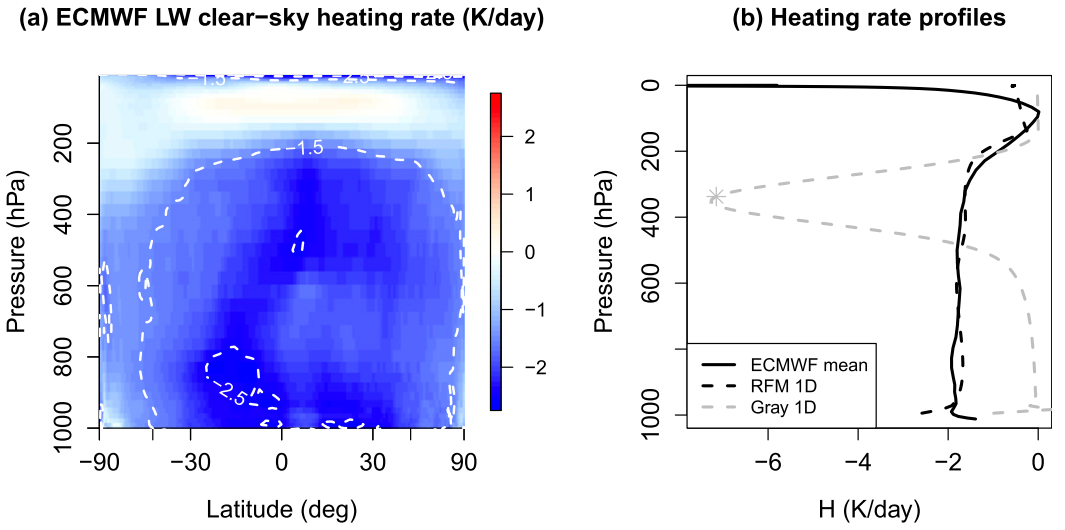

FIG. 1. (a) Zonal mean clear-sky longwave heating rates $\mathscr{H}$ from ERA-Interim (Dee et al. 2011) for June–August 2001, calculated with RRTM (Morcrette et al. 1998; Mlawer et al. 1997). White contours are for $\mathscr{H} = -1.5$ and $-2.5\,\mathrm{K\,day^{-1}}$, and show that this range encompasses most of the troposphere. (b) Vertical heating rate profiles as calculated by globally averaging the ECMWF $\mathscr{H}$ (solid black line) and from our BASE atmosphere as calculated by RFM (dashed black line) and a gray model (dotted gray line) tuned to have the same column-integrated cooling as RFM (i.e., same area under the curve). Gray star denotes the $\tau = 1$ level for the gray model. The 1D RFM calculation emulates the tropospheric ECMWF global mean, but the 1D gray model fails dramatically.

profile by taking a meridional average (Fig. 1b, solid line). This profile has a characteristic value of $-2\,\mathrm{K\,day^{-1}}$ through most of the troposphere, and also exhibits the well-known "kink" around 200 hPa. This kink is significant, as it has been argued to constrain the altitude of clouds associated with both tropical convection [i.e., the fixed anvil temperature (FAT) hypothesis; Hartmann and Larson 2002; Hartmann et al. 2001] as well as extratropical baroclinic eddies (Thompson et al. 2017). In particular, the kink occurs at a characteristic temperature of roughly $T_{\mathrm{kink}} \approx 220\,\mathrm{K}$, and the FAT hypothesis argues that this should constrain convective anvil cloud fraction to also peak near T_{kink}, a prediction borne out broadly by cloud-resolving and general circulation models, as well as observations (Singh and O'Gorman 2015; Li et al. 2012; Harrop and Hartmann 2012; Eitzen et al. 2009; Kuang and Hartmann 2007; Kubar et al. 2007; Xu et al. 2007; Hartmann and Larson 2002).[2] Despite its importance, however, the kink has so far only been attributed qualitatively to a Clausius–Clapeyron (CC)-driven decline in "water vapor emissivity." In particular, we lack a quantitative theory for why $T_{\mathrm{kink}} \approx 220\,\mathrm{K}$, or for how this temperature scale might arise from CC scaling, which itself is exponential and thus is scale invariant.

Finally, another conspicuous feature of Fig. 1b is that above the kink one sees $\mathscr{H}$ declining toward zero, but then rebounding sharply in the stratosphere. It is well known that this strong stratospheric cooling emanates primarily from CO_2 molecules rather than H_2O (e.g., Zhu et al. 1992; Manabe et al. 1964), but we lack a simple explanation for how CO_2 cooling rates can be many times larger in the stratosphere than the troposphere, despite comparable temperature ranges in these two regions.

There are thus three basic questions we can ask about the $\mathscr{H}$ profile shown in Fig. 1b:

1) Why does it take on a characteristic value of $-2\,\mathrm{K\,day^{-1}}$, and why is this value relatively robust across the troposphere?
2) What causes the upper-tropospheric kink in $\mathscr{H}$, and why is T_{kink} constrained to be roughly 220 K?
3) Why is CO_2 cooling enhanced in the stratosphere relative to the troposphere?[3]

[2] For a recent critique of these claims, however, see Seeley et al. (2019a,b).

[3] Note that the strong longwave stratospheric cooling rates are themselves fixed by the need to balance strong shortwave heating by ozone, so this question is really about how CO_2 exhibits such strong cooling in a stratosphere that is not significantly warmer than the troposphere.

The goal of this paper is to shed light on these questions. To do so, we will need to bridge the gap between the complex radiative transfer calculations used in Fig. 1 and simple gray models, which are still used in atmospheric modeling (see section 8) but are *too* simple in the sense that they do not reproduce the phenomena of interest. To bring this into focus, we first emulate the ECMWF $\mathscr{H}$ profile in Fig. 1b with the $\mathscr{H}$ profile of an idealized atmospheric column with H_2O only and a constant lapse rate and constant relative humidity, as calculated with the comprehensive line-by-line Reference Forward Model (RFM; dashed line of Fig. 1b; further details of this BASE case in section 2a). This profile emulates the tropospheric global average ECMWF profile quite well. Despite the relative simplicity of our single atmospheric column, however, this RFM calculation is still too complex to provide much understanding, as it still convolves intricate greenhouse gas spectroscopy with radiative transfer.

If we instead turn to a gray radiation model tuned to yield the same column-integrated cooling as the RFM profile,[4] we find instead that the gray model cannot emulate the RFM and ECMWF profiles: the gray radiative cooling profile has far too much vertical structure, and its upper-tropospheric heating rates err by a factor of 3 or more [Fig. 1b, gray line; see also Fig. S1 of Seeley et al. (2019b)]. There is thus indeed a gap between our simulation and understanding of radiative cooling, and answering the questions posed above will require bridging this gap.

To accomplish this, we will consider spectral radiation, but will simplify greenhouse gas spectroscopy by approximating the absorption spectrum of our greenhouse gases as piecewise exponentials, following Wilson and Gea-Banacloche (2012). We will also simplify the radiative transfer by invoking the cooling-to-space approximation (e.g., Jeevanjee and Fueglistaler 2020; Petty 2006; Green 1967; Rodgers and Walshaw 1966). These simplifications lead to a succession of simple spectral models, the two-dimensional simple spectral model (SSM2D) and one-dimensional simple spectral model (SSM1D), constructed in section 3. These models exhibit the phenomena of interest in questions 1–3 above but are analytically tractable, and are thus used to address those questions in sections 4–7. We conclude in section 8.

2. Preliminaries

Before building models of radiative cooling we must first lay some groundwork. In this section we detail the line-by-line calculations that we use as a benchmark, then present a qualitative picture of spectrally resolved radiative cooling, and finally review the physics of the cooling-to-space approximation.

a. *RFM calculations*

All line-by-line calculations in this paper are performed with the RFM (Dudhia 2017). We use High-Resolution Transmission (HITRAN) 2016 spectroscopic data for the most common isotopologue of H_2O and CO_2 from 10 to 1500 and from 500 to 850 cm^{-1}, respectively. For our BASE case we consider an idealized atmosphere with H_2O as the only greenhouse gas, surface temperature $T_s = 300\,\mathrm{K}$, a constant lapse rate of $\Gamma = 7\,\mathrm{K\,km}^{-1}$ up to an isothermal stratosphere at $T_{\mathrm{strat}} = 200\,\mathrm{K}$, a tropospheric relative humidity (RH) of 0.75, and a stratospheric H_2O concentration of 23 ppmv (corresponding to an RH of 0.75 at the tropopause, and relatively large due to the 200-K tropopause). We run RFM at a spectral resolution of $0.1\,\mathrm{cm}^{-1}$ and a uniform vertical resolution of 100 m up to model top at 50 km. We output optical depth, fluxes, heating rates, and absorption coefficients, all as a function of wavenumber and height. For simplicity in comparing to our analytical model below, RFM optical depth is calculated along a vertical path (zenith angle of zero), and fluxes and heating rates are computed using a two-stream (rather than RFM's default four-stream) approximation with a diffusivity factor of $D = 1.5$ [as specified in Dudhia (2017), following Clough et al. (1992)].[5] In BASE we omit the water vapor continuum (Shine et al. 2012), not because it is negligible but simply for analytic tractability. The effects of the water vapor continuum, as parameterized in RFM (using the MT_CKD continuum; Mlawer et al. 2012) are considered in appendix A.

b. *The shape of* $\mathscr{H}_{\tilde{\nu}}$

The object of interest in this paper is the familiar clear-sky longwave radiative heating $\mathscr{H}$. But $\mathscr{H}$ is the spectral integral of the less familiar spectrally resolved heating:

$$\mathscr{H}_{\tilde{\nu}} \equiv \frac{g}{C_p}\partial_p F_{\tilde{\nu}} \quad (\mathrm{K\,s^{-1}\,cm}), \tag{1}$$

[4] More precisely, we use the same thermodynamic profiles and absorber concentration as the RFM calculation, but use a non-pressure-broadened gray absorption coefficient tuned to yield the same column-integrated radiative cooling (of roughly $170\,\mathrm{W\,m}^{-2}$) as the RFM calculation.

[5] For reproducibility, note also that we run RFM with the BFX flag disabled. This means the Planck function is assumed constant within an RFM vertical grid cell, rather than assuming a subgrid vertical variation of the Planck function that is linear in height.

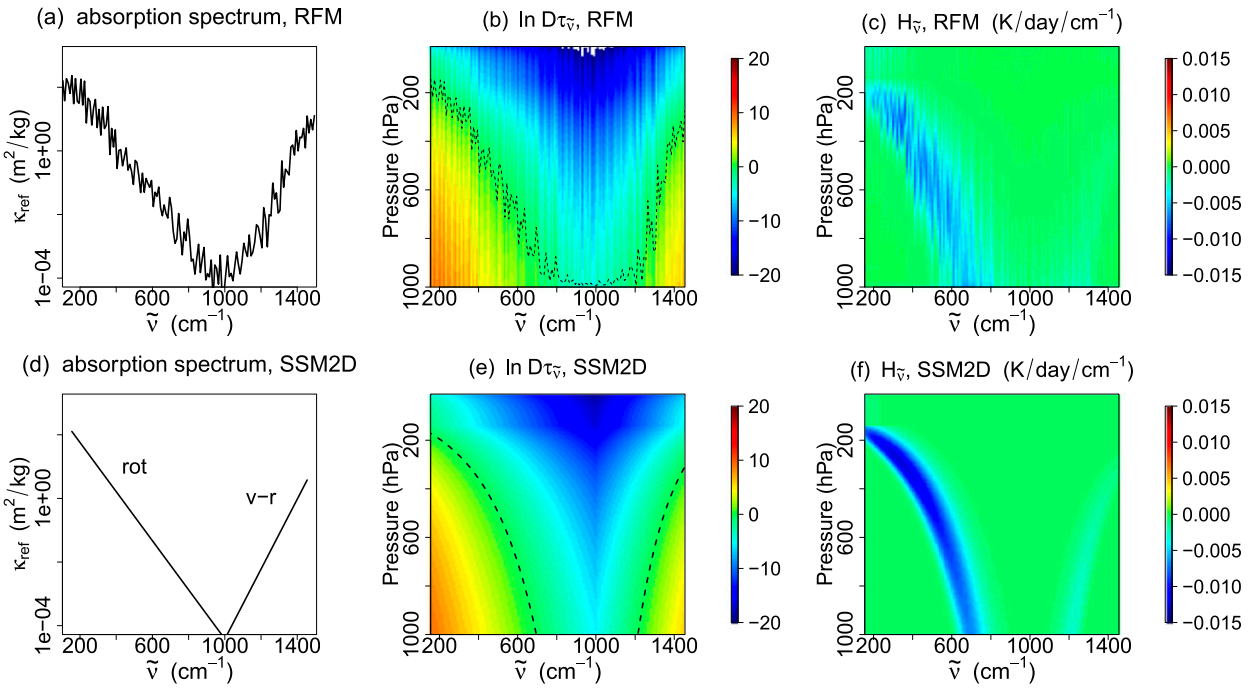

FIG. 2. Comparison between RFM output and the SSM2D, as follows: (a),(d) H_2O absorption spectrum κ_{ref} at $(T_{\text{ref}}, p_{\text{ref}}) = (260\,\text{K}, 500\,\text{hPa})$ from RFM and our linear fit Eq. (10), respectively. (b),(e) Logarithm of diffusion coefficient D times optical depth $\tau_{\tilde{\nu}}$ from RFM and Eq. (12), respectively, along with $\tau_{\tilde{\nu}} = 1$ contours. (c),(f) Spectrally resolved heating $\mathscr{H}_{\tilde{\nu}}$ from RFM and the SSM2D [Eqs. (5) and (12)]. All RFM plots show averages over 10-cm^{-1} bins, with log averaging in (a) and linear averaging in (b) and (c). The plots in(a)–(c) show that the spectrally resolved cooling $\mathscr{H}_{\tilde{\nu}}$ can be understood as emission from $\tau_{\tilde{\nu}} = 1$ levels, where the height of these levels is determined by $\kappa_{\text{ref}}(\tilde{\nu})$. The plots in (d)–(f) show that the SSM2D captures this physics.

where $\tilde{\nu}$ denotes wavenumber (following the notation of Petty 2006; Thomas and Stamnes 2002; Houghton 2002) and $F_{\tilde{\nu}}$ denotes spectrally resolved net upward LW flux ($\text{W m}^{-2}\,\text{cm}^{-1}$). Thus, any understanding of $\mathscr{H}$ must stem from an understanding of $\mathscr{H}_{\tilde{\nu}}$. Before pursuing a quantitative model for $\mathscr{H}_{\tilde{\nu}}$ (as in the next section), we should first develop a qualitative picture of the physics of $\mathscr{H}_{\tilde{\nu}}$, and understand how it leads to the familiar $\mathscr{H}$ profiles of Fig. 1b. We do this now, following the treatment of, for example, Harries et al. (2008) and Clough et al. (1992).

Figure 2c shows $\mathscr{H}_{\tilde{\nu}}$ from BASE as computed by RFM. There is a strong band of cooling for $\tilde{\nu} < 800\,\text{cm}^{-1}$, and a much weaker band for $\tilde{\nu} > 1200\,\text{cm}^{-1}$. To understand these structures, we consider the optical depth $\tau_{\tilde{\nu}}$, measured from $p = 0$ and given by

$$\tau_{\tilde{\nu}}(p) \equiv \int_0^p \underbrace{\kappa(\tilde{\nu}, T, p')}_{\text{m}^2\,\text{kg}^{-1}} \underbrace{q_v \frac{dp'}{g}}_{\text{kg m}^{-2}}. \tag{2}$$

Here q_v is water vapor specific humidity (kg kg^{-1}) and the mass absorption coefficient κ ($\text{m}^2\,\text{kg}^{-1}$) depends not only on wavenumber $\tilde{\nu}$ but also on T and p, due to temperature scaling and pressure broadening (Pierrehumbert 2010).[6] All other symbols have their usual meaning. Note that since κ is an effective area per unit mass, and since the rest of the integrand in Eq. (2) is just the mass per unit area of absorber above level p (i.e., the pathlength), $\tau_{\tilde{\nu}}$ can be interpreted as the effective area of absorbers above level p per unit geometric area (see also Jeevanjee 2018).

The spectral distribution of optical depth as output from RFM is shown in Fig. 2b, which also plots the $\tau_{\tilde{\nu}} = 1$ levels for each $\tilde{\nu}$. The two diagonal bands in the $\mathscr{H}_{\tilde{\nu}}$ plot correspond to two diagonal $\tau_{\tilde{\nu}} = 1$ bands, which is where we expect emission to space at a given $\tilde{\nu}$ to maximize (Jeevanjee and Fueglistaler 2020; Wallace and Hobbs 2006; Petty 2006; see also gray line in Fig. 1b, and section 2c below). The shape of these $\tau_{\tilde{\nu}} = 1$ bands in the $\tilde{\nu}$–p plane can themselves be understood in terms of reference absorption coefficients:

[6] Both temperature scaling and pressure broadening are second-order effects on κ, relative to its wavenumber dependence. At the same time, neglecting pressure broadening entirely leads to results whose inaccuracy we found unacceptable, so we include pressure broadening in our simple models below. Temperature scaling, on the other hand, is omitted.

$$\kappa_{\text{ref}}(\tilde{\nu}) \equiv \kappa(\tilde{\nu}, T_{\text{ref}}, p_{\text{ref}}), \tag{3}$$

where we take

$$(T_{\text{ref}}, p_{\text{ref}}) = (260\,\text{K}, 500\,\text{hPa}), \tag{4}$$

roughly in the middle of the BASE troposphere. These κ_{ref} coefficients, also output from RFM and coarse-grained over $10\,\text{cm}^{-1}$ bins, are shown in Fig. 2a. The two $\tau_{\tilde{\nu}} = 1$ bands in Fig. 2b correspond to the two absorption bands evident in the κ_{ref} plot: the pure rotation band ($\tilde{\nu} < 1000\,\text{cm}^{-1}$), and the vibration-rotation band ($1000 < \tilde{\nu} < 1450\,\text{cm}^{-1}$). By Eq. (2), where κ_{ref} is relatively large then $\tau_{\tilde{\nu}} = 1$ occurs at relatively high altitudes, and vice versa, so that plots of κ_{ref} and $\tau_{\tilde{\nu}} = 1$ levels necessarily have the same shape. This shape also manifests in the $\mathscr{H}_{\tilde{\nu}}$ field. These multiple manifestations of H_2O spectroscopy can all be seen in the top row of Fig. 2, and understanding these interrelations between κ_{ref}, $\tau_{\tilde{\nu}}$, and $\mathscr{H}_{\tilde{\nu}}$ is critical for what follows.

Note that the physics described here also explains why the gray model fails so dramatically in emulating the RFM $\mathscr{H}$ profile in Fig. 1b: a gray model has a single κ_{ref} value and can thus only reach $\tau = 1$ at one height, around which $\mathscr{H}$ will peak. Real greenhouse gas spectroscopy, on the other hand, yields a distribution of κ_{ref} values and hence a distribution of $\tau = 1$ heights (Figs. 2a,b), each of which contribute to $\mathscr{H}$ and hence yield a much more uniform $\mathscr{H}$ profile.

c. *The cooling-to-space approximation and the transmissivity gradient*

Strictly speaking, the $\tau = 1$ law invoked above applies only to the emission of OLR (or "cooling to space"), not radiative heating rates per se. This is because heating rates include not just cooling to space, but also radiative exchange between atmospheric layers as well as the surface (Green 1967). However, these "exchange terms" are often negligible (Jeevanjee and Fueglistaler 2020; Clough et al. 1992; Rodgers and Walshaw 1966), so radiative cooling may indeed be approximated solely by the cooling-to-space term. This yields the *cooling-to-space approximation*:

$$\partial_p F_{\tilde{\nu}} \approx \pi B(\tilde{\nu}, T) \frac{\partial \mathscr{T}_{\tilde{\nu}}}{\partial p}. \tag{5}$$

Here $\mathscr{T}_{\tilde{\nu}} \equiv \exp(-\tau_{\tilde{\nu}})$ is the transmission function and $\pi B(k, T)(\partial \mathscr{T}_{\tilde{\nu}}/\partial p)$ is the cooling-to-space (CTS) term in pressure coordinates. This is the differential contribution of an atmospheric layer to the OLR at wavenumber $\tilde{\nu}$, and is given by Planck emission $\pi B(\tilde{\nu}, T)$ times the transmissivity gradient $\partial_p \mathscr{T}_{\tilde{\nu}}$. A key feature of the CTS approximation Eq. (5) is that the CTS term can be computed *without* solving the radiative transfer equations for the net flux $F_{\tilde{\nu}}$; this fact greatly simplifies our formalism, and has even been leveraged in the past in numerical radiative transfer schemes (Dufresne et al. 2005; Joseph and Bursztyn 1976; Fels and Schwarzkopf 1975).

How should one think about and evaluate the transmissivity gradient in Eq. (5)? For this purpose, it is convenient to define the optical depth exponent β,

$$\beta \equiv \frac{\partial \ln \tau_{\tilde{\nu}}}{\partial \ln p}. \tag{6}$$

We will see below that β is constant in the vertical for CO_2, and roughly constant for H_2O.[7] We can use β to write the transmissivity gradient as

$$\frac{\partial \mathscr{T}_k}{\partial p} = -\frac{\beta}{p} \tau_{\tilde{\nu}} e^{-\tau_{\tilde{\nu}}}. \tag{7}$$

The factor $\beta/p = \partial_p \ln \tau_{\tilde{\nu}}$ is an inverse "scale pressure" for optical depth, and measures the rate at which $\tau_{\tilde{\nu}}$ increases with pressure by one e-folding. The other factor $\tau_{\tilde{\nu}} e^{-\tau_{\tilde{\nu}}}$ is a kind of "weighting function" that peaks at $\tau_{\tilde{\nu}} = 1$, thus giving rise to the $\tau = 1$ law.[8] Thus, the peak magnitude of Eq. (7) can be estimated by evaluation at $\tau_{\tilde{\nu}} = 1$:

$$\left.\frac{\partial \mathscr{T}_k}{\partial p}\right|_{\tau_{\tilde{\nu}}=1} = -\frac{1}{e}\frac{\beta}{p}. \tag{8}$$

We thus have the key result that β/p governs the peak magnitude of the transmissivity gradient. As such, this quantity will appear frequently throughout this paper.[9] In particular, the variations in β/p between CO_2 and H_2O, and between troposphere and stratosphere, will play a significant role in answering question 3 in section 7.

As a caveat, note that even though the CTS approximation and the accompanying $\tau = 1$ law appear to hold quite well for Earth's atmosphere, these rules are not entirely general. The CTS approximation fails in the textbook case of pure gray radiative equilibrium (which has zero radiative cooling everywhere; Pierrehumbert 2010), and turns out to also depend on the choice of vertical coordinate. These issues, as well as more general

[7] There is also a slight wavenumber dependence of β (standard deviation of ±20% across wavenumber space) that we neglect.

[8] Strictly speaking one also needs to worry about the vertical variations in $1/p$ as well as the Planck function in Eq. (7), but these turn out to compensate each other (Jeevanjee and Fueglistaler 2020).

[9] This is one reason why we choose to write Eq. (7) in its particular form, with a mix of p and $\tau_{\tilde{\nu}}$ coordinates. Another reason is that the form of Eq. (7) is amenable to the analytical spectral integration we perform in section 3b.

criteria for the CTS approximation (and the $\tau = 1$ law) to hold, are the subject of the companion paper Jeevanjee and Fueglistaler (2020).

3. Simple spectral models for H_2O cooling

a. *SSM2D: A model for spectrally resolved cooling $\mathscr{H}_{\tilde{\nu}}$*

Having laid the necessary groundwork, we now turn to building a simple model for spectrally and vertically resolved heating rates $\mathscr{H}_{\tilde{\nu}}$, focusing for the moment on H_2O. Since the model has two resolved dimensions ($\tilde{\nu}$ and p), we will refer to it as our SSM2D.

The first step in building the SSM2D for H_2O is to simplify H_2O spectroscopy, that is, the functional form of H_2O mass absorption coefficients $\kappa_{\text{ref}}(\tilde{\nu})$ (Fig. 2a). We follow Wilson and Gea-Banacloche (2012) and first coarse grain $\ln\kappa_{\text{ref}}(\tilde{\nu})$ over spectral intervals of $10\,\text{cm}^{-1}$ (this is already what is plotted in Fig. 2a). We then delineate the H_2O rotation band (rot) and vibration–rotation band (v-r) as[10]

$$\begin{aligned} &\text{rot: } \tilde{\nu}_{\text{rot}} \equiv 150 < \tilde{\nu} < 1000\,\text{cm}^{-1} \\ &\text{v-r: } 1000 < \tilde{\nu} < 1450\,\text{cm}^{-1} \equiv \tilde{\nu}_{\text{v-r}}. \end{aligned} \tag{9}$$

We then apply a linear fit to $\ln\kappa_{\text{ref}}(\tilde{\nu})$ within each band to obtain a piecewise exponential approximation for $\kappa_{\text{ref}}(\tilde{\nu})$:

$$\kappa_{H_2O}(\tilde{\nu}) \equiv \begin{cases} \kappa_{\text{rot}} \exp\left(-\dfrac{\tilde{\nu} - \tilde{\nu}_{\text{rot}}}{l_{\text{rot}}}\right) & \text{for } \tilde{\nu} \text{ in rot} \\ \kappa_{\text{v-r}} \exp\left(-\dfrac{\tilde{\nu}_{\text{v-r}} - \tilde{\nu}}{l_{\text{v-r}}}\right) & \text{for } \tilde{\nu} \text{ in v-r} \end{cases}. \tag{10}$$

The parameters $\ln\kappa_{\text{rot}}$ and $\ln\kappa_{\text{v-r}}$ are obtained as the maxima of the corresponding straight line fits, and l_{rot} and $l_{\text{v-r}}$ as the corresponding slopes. These parameter values are tabulated in Table 1, which also includes other symbol definitions. The l parameters have units of cm^{-1}, and describe how fast κ_{ref} exponentially declines with $\tilde{\nu}$ away from the band maximum. These parameters, and their analogs for CO_2, will turn out to play a crucial role in what follows.

With the simplified absorption spectra Eq. (10) in hand we can now construct simplified expressions for H_2O optical depth $\tau_{\tilde{\nu}}$. This is done using the analytical expression for vertically resolved water vapor path (WVP; $\text{kg}\,\text{m}^{-2}$) from SI Eq. (2) of Koll and Cronin (2018), except we consider an unsaturated atmosphere, replace the T factor out front with an average tropospheric temperature $T_{\text{av}} = (T_s + T_{\text{strat}})/2$ (results are not sensitive to this approximation), and consider an arbitrary lapse rate Γ. This yields

$$\text{WVP} = \underbrace{\frac{T_{\text{av}}\text{RH}p_v^{\infty}}{\Gamma L}}_{\text{WVP}_0} \exp\left(-\frac{L}{R_v T}\right), \tag{11}$$

where WVP_0 is a constant with units of WVP, $p_v^{\infty} = 2.5 \times 10^{11}$ Pa is a reference value for the saturation vapor pressure p_v^* where $p_v^*(T) = p_v^{\infty}\exp(-L/R_v T)$, and all other symbols have their usual meaning.

Combining this expression for water vapor path with an approximate pressure-broadening factor p/p_{ref}, as well as a diffusivity factor $D = 1.5$ to account for the two-stream approximation, we obtain the following approximation to Eq. (2) for H_2O:

$$\tau_{\tilde{\nu}} = D\kappa_{H_2O}(\tilde{\nu})\frac{p}{p_{\text{ref}}}\text{WVP}_0 \exp\left(-\frac{L}{R_v T}\right). \tag{12}$$

Substituting Eq. (12) into the CTS approximation Eq. (5) then yields an approximation for $\mathscr{H}_{\tilde{\nu}}$. This $\mathscr{H}_{\tilde{\nu}}$, along with the fitted κ_{H_2O} of Eq. (10) and optical depth $\tau_{\tilde{\nu}}$ of Eq. (12), constitute the SSM2D. These fields are shown in the bottom row of Fig. 2, directly underneath their RFM counterparts for easy comparison. For all three fields, the SSM2D captures the gross behavior of the RFM calculation.

At the same time, of course, the SSM2D neglects all finescale spectral structure. One drawback of this is that the SSM2D overestimates the peak values of $\mathscr{H}_{\tilde{\nu}}$ (Figs. 2c,f). This occurs because the finescale structure in the RFM calculation, when combined with a coarse graining into 10-cm^{-1} bins as we have done here, yields an $\mathscr{H}_{\tilde{\nu}}$ field that is "smeared out" in the $\tilde{\nu}$–p plane, such that the cooling around a given ($\tilde{\nu}$, p) occurs over a larger ($\tilde{\nu}$, p) range in RFM than in the SSM2D, and must thus have a smaller magnitude in RFM.

These errors are analyzed further in appendix B, where it is shown that they are not fundamental and indeed largely cancel upon spectral or vertical integration. The SSM2D thus produces reasonable values for the spectrally integrated cooling $\mathscr{H}$, as we will see below. Given this, the SSM2D could be used at this point to try and answer questions 1–3 posed above. However, further insight can be gained by making additional approximations and analytically integrating the $\mathscr{H}_{\tilde{\nu}}$ field over wavenumber space. We turn to this next.

[10] These wavenumber ranges were chosen to optimize the piecewise exponential fit in Eq. (10). With these choices, however, the SSM2D neglects wavenumbers less than $150\,\text{cm}^{-1}$. These wavenumbers turn out to make a negligible contribution to heating rates (not shown), presumably due to their low values of the Planck function, but their contribution is nonetheless included in all spectrally integrated RFM calculations in this paper.

TABLE 1. Definition of important symbols used throughout the paper (top section). Spectroscopic parameters used in the SSM2D and SSM1D (bottom section). The $\tilde{\nu}_{\text{rot}}$ and $\tilde{\nu}_{\text{v-r}}$ parameters are chosen by inspection of Fig. 2a, and $\tilde{\nu}_Q$ is chosen to be proximate to the central 667.66-cm^{-1} Q branch line. The κ and l parameters, on the other hand, are not externally specified but result from fits to RFM output. See text for details.

Quantity	Symbol	Units
Wavenumber	$\tilde{\nu}$	cm^{-1}
Mass absorption coefficient (with T, p dependence)	κ	m^2 kg^{-1}
Reference mass absorption coefficients (at $T_{\text{ref}} = 260$ K, $p_{\text{ref}} = 500$ hPa)	κ_{ref}, $\kappa_{\text{H}_2\text{O}}$, κ_{CO_2}	m^2 kg^{-1}
Optical depth at wavenumber $\tilde{\nu}$	$\tau_{\tilde{\nu}}$	—
Transmissivity at wavenumber $\tilde{\nu}$	$\mathscr{T}_{\tilde{\nu}} \equiv \exp(-\tau_{\tilde{\nu}})$	—
Optical depth exponent	$\beta \equiv \dfrac{d\ln\tau_{\tilde{\nu}}}{d\ln p}$	—
Planck function at wavenumber $\tilde{\nu}$, temperature T	$B(\tilde{\nu},\ T)$	W m^{-2} sr^{-1} cm
Clear-sky longwave heating rate	$\mathscr{H}$	K day^{-1}
Spectrally resolved clear-sky longwave heating rate	$\mathscr{H}_{\tilde{\nu}}$	K day^{-1} cm^{-1}
Diffusion coefficient for two-stream approximation	D	—
Reference water vapor path	WVP_0	kg m^{-2}
Spectroscopic band	j, denotes rot, v-r, or Q	—
$\tau_{\tilde{\nu}} = 1$ wavenumber profile in band j	$\tilde{\nu}_{1,j}(p)$	cm^{-1}
Heating rate integrated over band j	$\mathscr{H}_j$	K day^{-1}
Effective emitting width	$\Delta\tilde{\nu}$	cm^{-1}
Spectrally integrated transmissivity gradient	$\dfrac{\partial\mathscr{T}_{\tilde{\nu}}}{\partial p}$	cm^{-1} hPa^{-1}
SSM spectroscopy parameters	H_2O	CO_2
Wavenumbers at band maxima	$\tilde{\nu}_{\text{rot}} = 150$ cm^{-1} $\tilde{\nu}_{\text{v-r}} = 1450$ cm^{-1}	$\tilde{\nu}_Q = 667.5$ cm^{-1}
Band-maximum reference absorption coefficients	$\kappa_{\text{rot}} = 127$ m^2 kg^{-1} $\kappa_{\text{v-r}} = 3.8$ m^2 kg^{-1}	$\kappa_Q = 110$ m^2 kg^{-1}
Spectroscopic decay parameter	$l_{\text{rot}} = 56$ cm^{-1} $l_{\text{v-r}} = 40$ cm^{-1}	$l_Q = 11.5$ cm^{-1}

b. *SSM1D: A model for spectrally integrated cooling $\mathscr{H}$*

We now construct an SSM1D for spectrally integrated cooling $\mathscr{H}$. Our starting point will be the SSM2D for $\mathscr{H}_{\tilde{\nu}}$, which itself is still too complicated to be analytically integrated over wavenumber space, so further approximations will be required. (The SSM1D is thus *not* equivalent to simply integrating the SSM2D numerically over wavenumber space, though we will employ this latter quantity later on as well.) To proceed we need two more derived quantities. The first is an expression for β for H_2O, which we obtain by substituting our expression (12) for $\tau_{\tilde{\nu}}$ into the definition (6) of β:

$$\beta_{\text{H}_2\text{O}} = 1 + \frac{L}{R_v T}\frac{\Gamma R_d}{g}. \tag{13}$$

Typical tropospheric values[11] for $\Gamma = 7$ K km^{-1} are $\beta_{\text{H}_2\text{O}} = 5.5 \pm 1$.

[11] In the tropics, where Γ is set by the moist adiabat and is roughly 4 K km^{-1} near the surface and 9 K km^{-1} in the upper troposphere, the variation in β is larger: $\beta_{\text{H}_2\text{O}} \approx 5.5 \pm 2$.

The second (and more important) derived quantity is the wavenumber profile $\tilde{\nu}_{1,j}(p)$, which parameterizes the $\tau_{\tilde{\nu}} = 1$ contour in the $\tilde{\nu}$–p plane for band j and hence gives the corresponding locus of cooling in the $\tilde{\nu}$–p plane [here j denotes either the rot or v-r bands from Eq. (9)]. We obtain analytical expressions for $\tilde{\nu}_{1,j}$ by substituting $\kappa_{\text{H}_2\text{O}}$ from Eq. (10) into the $\tau_{\tilde{\nu}}$ formula in (12), setting $\tau_{\tilde{\nu}} = 1$, and solving for $\tilde{\nu}$ in each band, yielding

$$\tilde{\nu}_{1,\text{rot}} = \tilde{\nu}_{\text{rot}} + l_{\text{rot}}\left[\ln(D\kappa_{\text{rot}}\text{WVP}_0) + \ln(p/p_{\text{ref}}) - \frac{L}{R_v T}\right],$$
$$\tilde{\nu}_{1,\text{v-r}} = \tilde{\nu}_{\text{v-r}} - l_{\text{v-r}}\left[\ln(D\kappa_{\text{v-r}}\text{WVP}_0) + \ln(p/p_{\text{ref}}) - \frac{L}{R_v T}\right]. \tag{14}$$

These $\tau = 1$ contours are overlaid over the simple $\tau_{\tilde{\nu}}$ distribution in Fig. 2e, and capture the overall shape and x and y intercepts of the noisier $\tau = 1$ contours diagnosed from RFM output (Fig. 2b). Note that the exponentials in $\kappa_{\text{H}_2\text{O}}(k)$ and $\exp(-L/R_v T)$ cancel out when solving Eq. (12) for $\tilde{\nu}_{1,j}$, so that $\tilde{\nu}_{1,j}$ has a relatively strong $1/T$ temperature dependence and only a logarithmic dependence on other variables. This will be of significance in section 5.

With these ingredients in place we now obtain an analytical approximation for the spectrally integrated heating in band j, denoted $\mathscr{H}_j$. We begin by integrating Eq. (1) over band j at a given p, assuming the limits of the spectral integral are implicitly given by the appropriate wavenumber range from Eq. (9). We also invoke the CTS approximation Eq. (5) as well as Eq. (7). This yields

$$\mathscr{H}_j = -\frac{g}{C_p}\frac{\beta}{p}\int d\tilde{\nu}\, \pi B(\tilde{\nu}, T)\tau_{\tilde{\nu}}\exp(-\tau_{\tilde{\nu}}). \tag{15}$$

To evaluate this integral, recall that the function $\tau_{\tilde{\nu}}\exp(-\tau_{\tilde{\nu}})$ peaks at $\tau_{\tilde{\nu}} = 1$ (with corresponding wavenumber $\tilde{\nu}_{1,j}$), and that its integral $\int_0^\infty d\tau_{\tilde{\nu}}\,\tau_{\tilde{\nu}}\exp(-\tau_{\tilde{\nu}}) = 1$. These properties are shared by the Dirac delta function $\delta(\tau_{\tilde{\nu}} - 1)$, so we might approximate $\tau_{\tilde{\nu}}\exp(-\tau_{\tilde{\nu}})$ by $\delta(\tau_{\tilde{\nu}} - 1)$. This approximation can be applied to Eq. (15) once we convert $\delta(\tau_{\tilde{\nu}} - 1)$ to a delta function in $\tilde{\nu}$ coordinates, using the appropriate chain rule (e.g., Gasiorowicz 2003) as well as Eqs. (12) and (10):

$$\delta(\tau_{\tilde{\nu}} - 1) = \left|\frac{\partial\tau_{\tilde{\nu}}}{\partial\tilde{\nu}}(\tilde{\nu}_{1,j})\right|^{-1}\delta(\tilde{\nu} - \tilde{\nu}_{1,j}) = l_j\delta(\tilde{\nu} - \tilde{\nu}_{1,j}).$$

Note the appearance of the l_j parameter here, which we comment on further below. Plugging this last equation into Eq. (15) and performing the now trivial spectral integration yields finally our desired result, an analytic expression for bandwise integrated radiative cooling:

$$\mathscr{H}_j \approx -\frac{g}{C_p}\pi B(\tilde{\nu}_{1,j}, T)\frac{\beta}{p}l_j. \tag{16}$$

Note that $B(\tilde{\nu}_{1,j}, T)$ gives the Planck emission as a function of height *only,* since $\tilde{\nu}_{1,j}$ [cf. Eq. (14)] is a function of height, which gives the wavenumber that cools to space at a given height. Equation (16), along with its inputs from Eqs. (13) and (14), constitute the SSM1D.

4. Interpretation and estimation

a. Interpretation

The SSM1D Eq. (16) is a central result of this paper. How should we interpret it? From Eq. (8) we know that the β/p factor in Eq. (16) is closely related to the transmissivity gradient $\partial_p\mathscr{T}_{\tilde{\nu}}$ evaluated at $\tau_{\tilde{\nu}} = 1$. Furthermore, $-\partial_p\mathscr{T}_{\tilde{\nu}}$ can be interpreted as the "emissivity to space" gradient: for an atmospheric layer of thickness Δp we can interpret $-\Delta p\partial_p\mathscr{T}_{\tilde{\nu}} = \Delta p(d\tau_{\tilde{\nu}}/dp)\mathscr{T}_{\tilde{\nu}}$ as its "emissivity to space," since $\Delta p(d\tau_{\tilde{\nu}}/dp)$ gives the absolute emissivity of the layer and $\mathscr{T}_{\tilde{\nu}}$ is the fraction of emitted radiation that escapes to space. Thus $-\partial_p\mathscr{T}_{\tilde{\nu}}$ is the emissivity-to-space gradient (in pressure coordinates). This suggests that we rewrite Eq. (16) as

$$\mathscr{H}_j = -\frac{g}{C_p}\underbrace{\pi B(\tilde{\nu}_{1,j}, T)}_{\substack{\text{Planck}\\ \text{emission}\\ (\mathrm{W\,m^{-2}\,cm^{-1}})}}\underbrace{\left(\frac{1}{e}\frac{\beta}{p}\right)}_{\substack{\text{emissivity}\\ \text{gradient}\\ (1/\mathrm{Pa})}}\underbrace{(l_j e)}_{\substack{\text{spectral}\\ \text{width } \Delta\tilde{\nu}\\ (\mathrm{cm^{-1}})}}. \tag{17}$$

The factor $l_j e$ in Eq. (17) can be interpreted as an "effective emitting width" $\Delta\tilde{\nu}$, that is, as the width of the spectral region at any given height that is cooling to space. For the H_2O rot band we find $\Delta\tilde{\nu} = l_{\mathrm{rot}}e \approx 165\,\mathrm{cm^{-1}}$, in rough eyeball agreement with the width of the active cooling regions in Figs. 2c and 2f. That l_j simultaneously gives the inverse decay rate of $\kappa(\tilde{\nu})$ [Eq. (10)] as well as the effective emitting width $\Delta\tilde{\nu}$ may seem mysterious at first, but is consistent in that a larger decay rate for $\kappa(\tilde{\nu})$ implies a narrower peak of $\tau_{\tilde{\nu}}e^{-\tau_{\tilde{\nu}}}$ in $\tilde{\nu}$ coordinates in Eq. (15), and hence a smaller $\Delta\tilde{\nu}$. This quantitative connection between the spectroscopy of a greenhouse gas and its effective emitting width (and hence $\mathscr{H}_j$) is one of the major insights provided by the SSM1D.

In summary, then, Eq. (17) says that radiative heating at a given height may be interpreted as spectral Planck emission, times a spectral width, times an appropriate measure of emissivity, all evaluated at $\tilde{\nu}_{1,j}$ where $\tau_{\tilde{\nu}_{1,j}} = 1$. This yields a flux divergence (which in pressure coordinates has units of $\mathrm{W\,m^{-2}\,Pa^{-1}}$), which we multiply by g/C_p to get a heating rate in $\mathrm{K\,day^{-1}}$.

b. A back-of-the-envelope estimate of $\mathscr{H}$

A primary motivation for developing the SSM1D is to address question 1 from the introduction and make a back-of-the-envelope estimate of $\mathscr{H}$, which we now do. We use our BASE atmosphere and consider the reference level given in Eq. (4), which corresponds to $\tilde{\nu}_{1,\mathrm{rot}} = 500\,\mathrm{cm^{-1}}$ and $\tilde{\nu}_{1,\mathrm{v\text{-}r}} = 1350\,\mathrm{cm^{-1}}$. Evaluating $\pi B(\tilde{\nu}_{1,j}, T)$ there yields

$$\pi B(\tilde{\nu}_{1,\mathrm{rot}}, 260\,\mathrm{K}) \approx 0.3\,\mathrm{W\,m^{-2}\,cm},$$

$$\pi B(\tilde{\nu}_{1,\mathrm{v\text{-}r}}, 260\,\mathrm{K}) \approx 0.05\,\mathrm{W\,m^{-2}\,cm}.$$

Thus v-r Planck emission is roughly 1/6 of that for rot, which explains why the cooling in the v-r band in Figs. 2c and 2f is much smaller than that in the rot band. We thus neglect $\mathscr{H}_{\mathrm{v\text{-}r}}$ for this estimate, and also take $\beta_{H_2O} \approx 5$. We then have

$$\mathscr{H} \approx -\frac{g}{C_p}\pi B(\tilde{\nu}_{1,\mathrm{rot}}, T)\, l_{\mathrm{rot}} \frac{\beta_{\mathrm{H_2O}}}{p}$$
$$\approx -\left(10^{-4}\frac{\mathrm{K\,s^{-1}}}{\mathrm{W\,m^{-2}\,hPa^{-1}}}\right)(20\,\mathrm{W\,m^{-2}})\left(\frac{5}{500\,\mathrm{hPa}}\right)$$
$$= -2\times 10^{-5}\,\mathrm{K\,s^{-1}}$$
$$\approx -2\,\mathrm{K\,day^{-1}}. \quad (18)$$

Thus the SSM1D indeed allows us to quickly estimate the characteristic value $\mathscr{H} \approx -2\,\mathrm{K\,day^{-1}}$, using only fundamental constants, the atmospheric lapse rate (used in β), a typical value of the Planck function, and the RFM-derived parameter l_{rot}, which characterizes water vapor spectroscopy.

5. Validation and parameter sensitivities

We now seek to evaluate the SSM2D and SSM1D $\mathscr{H}$ profiles against the RFM benchmark, as well as gain insight into why the $-2\,\mathrm{K\,day^{-1}}$ value seems relatively robust across the troposphere (Fig. 1a and question 1 above). To this end, Fig. 3 shows $\mathscr{H}_{\mathrm{rot}} + \mathscr{H}_{\mathrm{v\text{-}r}}$ as calculated via RFM, SSM2D, and SSM1D. The SSM profiles (1D and 2D) track each other closely but underestimate cooling near the surface, an error due to the CTS approximation (Jeevanjee and Fueglistaler 2020). The SSM profiles also overestimate cooling in the upper troposphere and underestimate cooling in the stratosphere. Despite these errors and approximations, however, the tropospheric SSM profiles nonetheless lie in the characteristic $\sim 2 \pm 0.5\,\mathrm{K\,day^{-1}}$ range produced by comprehensive radiation calculations. The SSM profiles also both seem to reproduce the upper-tropospheric kink, which was the subject of question 2 above, and to which we return in section 6 below.

To further test the SSM1D, as well as understand the sensitivity of $\mathscr{H}$ to humidity and temperature variations, we perturb our atmospheric column. In one perturbation calculation we change RH from 0.75 to 0.3, and in another we change the lapse rate Γ from 7 to $5\,\mathrm{K\,km^{-1}}$. We run RFM and also evaluate the SSM1D on these two perturbed atmospheres, with the results shown in Figs. 4a and 4b (we cut off the RFM profiles at the same height that the SSM1D profiles go to zero, for clarity). Both the RFM and SSM1D profiles show a marked and perhaps surprising insensitivity to RH. Both models also show a reduction in cooling in the middle and lower troposphere of roughly 30% with the reduction in Γ (in the upper troposphere this signal becomes convolved with that from the differing upper-tropospheric temperatures). These relatively small sensitivities, which are consistent with the relative uniformity of clear-sky $\mathscr{H}$ across the globe (Fig. 1), can be understood using Eq. (16) as well

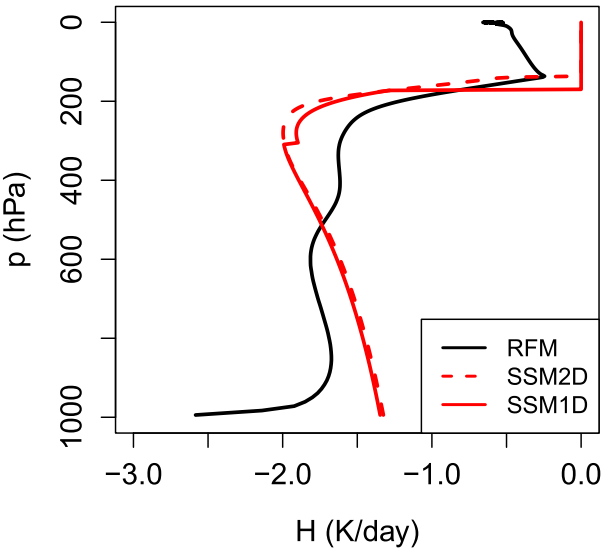

FIG. 3. Heating rate profiles calculated for our BASE case, using RMF, the SSM2D, and the SSM1D. Despite errors, the SSM2D and SSM1D capture the characteristic $-2 \pm 0.5\,\mathrm{K\,day^{-1}}$ magnitude of $\mathscr{H}$ from water vapor. See text for further discussion. Note that the water vapor continuum is turned off in the RFM BASE run.

as Eq. (14). These show that the change in RH only affects $\tilde{\nu}_{1,j}$, decreasing WVP_0 by roughly a factor of 2 and hence changing the $\tilde{\nu}_{1,j}$ by only $l_j \ln 2 \approx 35\,\mathrm{cm^{-1}}$, not enough to significantly change the Planck emission $B(\tilde{\nu}_{1,j},\ T)$. Changing Γ yields similarly small changes in $\tilde{\nu}_{1,j}$ but also has the additional effect of decreasing β; this is not negligible but is still a small change of roughly 30% [cf. Eq. (13)], leading to a similar reduction in $\mathscr{H}$ (physically, reducing the vertical temperature gradient lowers water vapor emissivity gradients because of Clausius–Clapeyron, which lowers the heating rate). Taken together, then, neither these RH or Γ variations (which are typical of such variations across the globe) significantly change the characteristic value of $\mathscr{H}$, because they are unable to significantly change Planck emission or vertical emissivity gradients (as encapsulated in β). This provides some insight into question 1 above. At the same time, of course, these perturbations are highly idealized, a point we return to in section 8. Also note that while our Γ perturbation does not change the characteristic value of $\mathscr{H}$, it does perturb the vertical structure and make $\mathscr{H}$ less vertically uniform, a point we return to below.

The final parameter to vary is T_s, which we vary across $T_s = (270, 280, 290, 300)\,\mathrm{K}$, leaving RH and Γ unchanged from BASE. The comparison of $\mathscr{H}$ for these atmospheres is shown in Figs. 4c and 4d. The RFM and the SSM1D $\mathscr{H}$ profiles behave similarly, with both weakening from roughly $-2\,\mathrm{K\,day^{-1}}$ at $T_s = 300\,\mathrm{K}$ to roughly $-1\,\mathrm{K\,day^{-1}}$ at $T_s = 270\,\mathrm{K}$. To the extent that the SSM1D captures this for the right reasons, Eq. (16) tells us

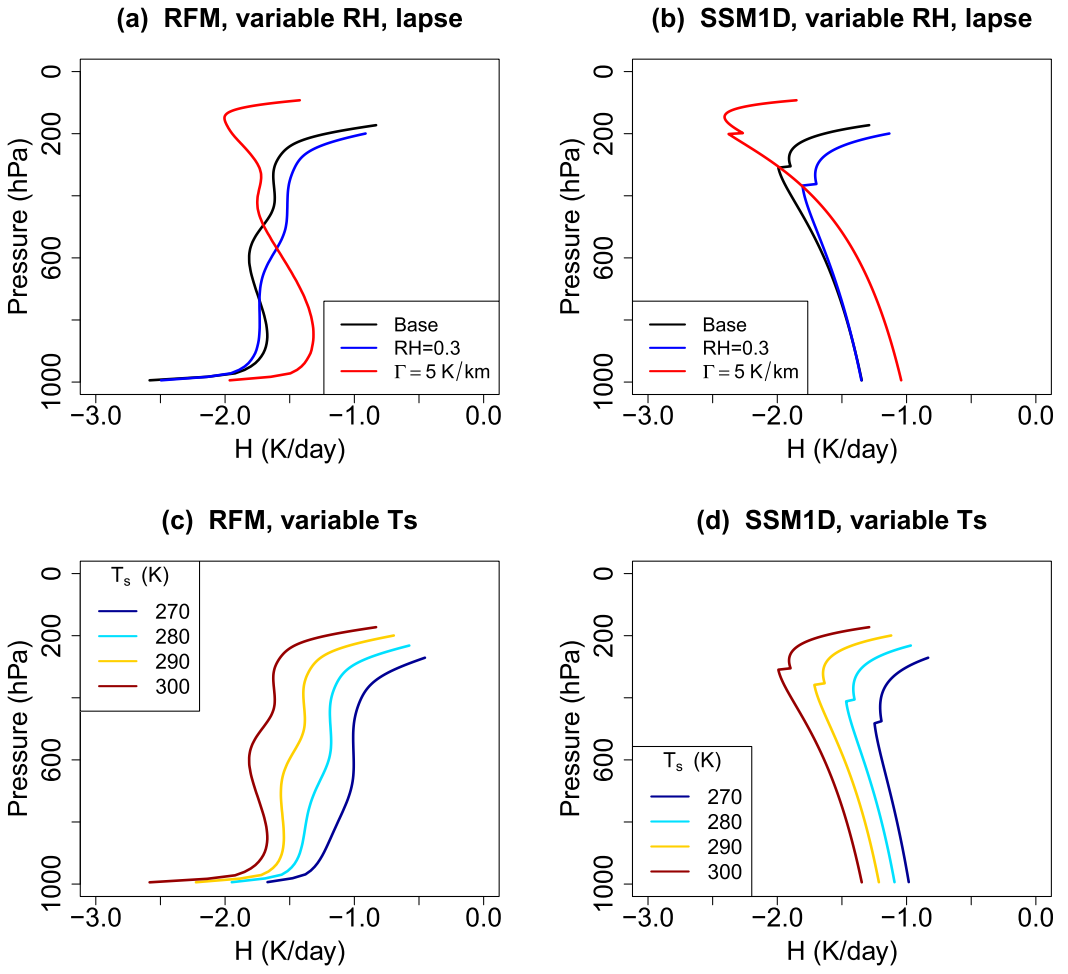

FIG. 4. (a) Profiles of $\mathscr{H}$ as output from RFM applied to BASE (black line), as well as atmospheric columns with RH = 0.3 (blue line) and $\Gamma = 5\,\mathrm{K\,km^{-1}}$ (red line). (b) As in (a), but computed from the SSM1D in Eq. (16). (c) As in (a), but for atmospheres with parameters as in BASE but with varying T_s. (d) As in (c), but computed from the SSM1D. All RFM profiles are cut off where the corresponding SSM1D profile cuts off for clarity of comparison. The characteristic value of $\mathscr{H}$ does not change significantly with these typical RH and Γ perturbations, but there is a systematic variation with T_s. These effects are exhibited by both RFM and the SSM1D.

that this must be due to a weakening Planck function (which, at fixed p, is being evaluated at both lower $\tilde{\nu}$ and lower T as T_s decreases). Both the RFM and SSM1D profiles also decrease in vertical extent with decreasing T_s, due to shoaling of the troposphere. These behaviors are also evident in the extratropical ECMWF $\mathscr{H}$ distribution in Fig. 1a, particularly in the Southern (winter) Hemisphere.

The foregoing explains to some degree the magnitude of latitudinal variations in $\mathscr{H}$, but does not explain the vertical uniformity of $\mathscr{H}$ profiles evident in Fig. 1. Some insight into this can also be gained from the SSM1D in Eq. (16), which tells us that this uniformity is largely coincidental, and arises from a cancellation between increasing transmissivity gradients (as encapsulated in β/p) and a declining Planck function $\pi B(\tilde{\nu}_{1j},\ T)$ with height. This suggests there is no fundamental constraint that $\mathscr{H}$ be uniform in the vertical; indeed, the SSM1D profile in Fig. 3 is noticeably less uniform than the RFM profile. Furthermore, even simply changing the lapse rate Γ is sufficient to make $\mathscr{H}$ notably less uniform, in both RFM and the SSM1D (Fig. 4). At the same time, of course, all of these profiles are much more vertically uniform than that from a gray model, as discussed in section 2b.

6. The upper-tropospheric kink

We now turn to question 2 above, about the origin of the upper-tropospheric kink in $\mathscr{H}$ and why $T_{\mathrm{kink}} \approx 220\,\mathrm{K}$. By Eq. (5), the two places to look for the origin of the kink are the Planck function $B(\tilde{\nu},\ T)$ and the transmissivity gradient $\partial_p \mathscr{T}_{\tilde{\nu}}$. Postponing discussion of $B(\tilde{\nu},\ T)$ for the moment, we begin by plotting $\partial_p \mathscr{T}_{\tilde{\nu}}$ for

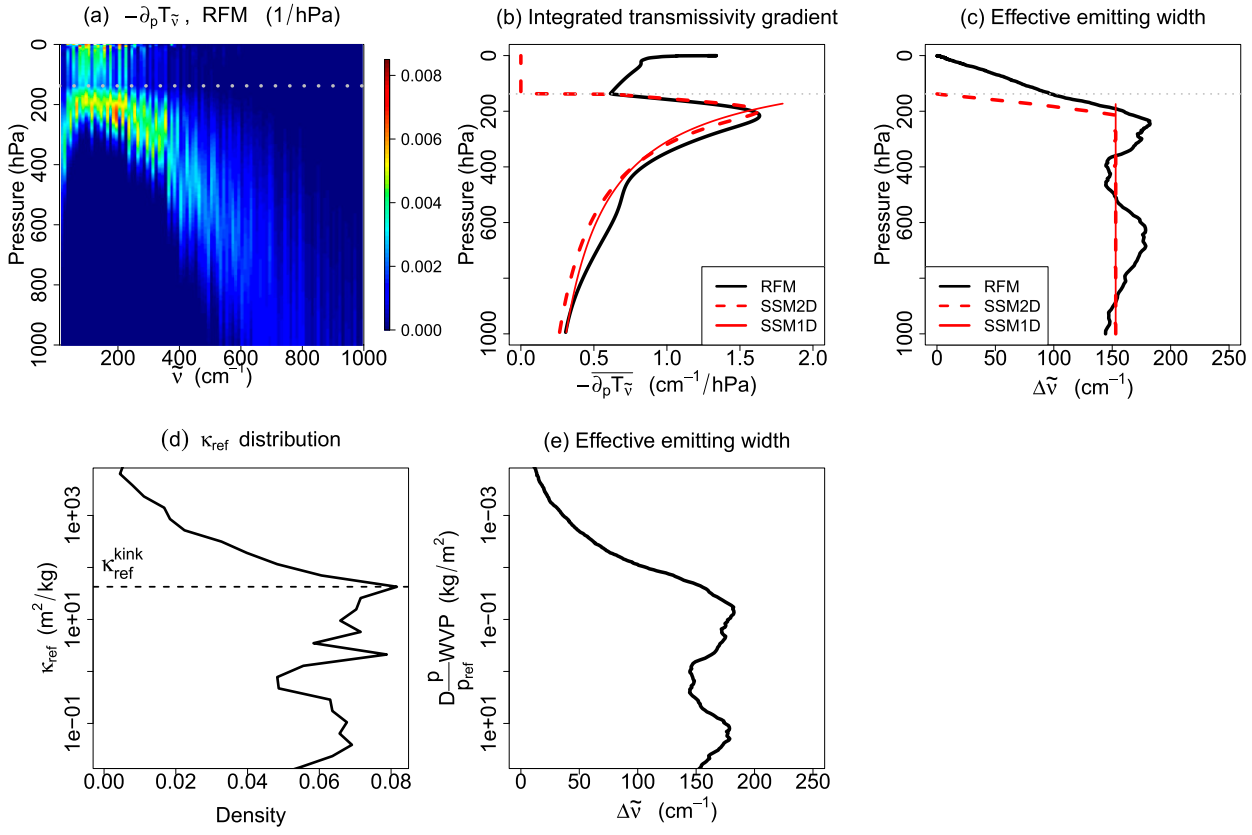

FIG. 5. (a) Transmissivity gradient $\partial_p \mathscr{T}_{\tilde{\nu}}$ for BASE as computed by RFM for the rot band only, averaged over 10-cm^{-1} bins. (b) Spectrally integrated transmissivity gradient $\overline{\partial_p \mathscr{T}_{\tilde{\nu}}}$ as defined in Eq. (19), computed via RFM and the SSM2D for the rot band and BASE atmosphere. Also shown is the SSM1D approximation to this quantity, given by $l_{rot}\beta/p$. The RFM and SSM2D profiles exhibit upper-tropospheric kinks coincident with their kinks in $\mathscr{H}$ (Fig. 3). (c) Effective emitting width $\Delta\tilde{\nu}$ as computed via Eq. (20). Both RFM and the SSM2D exhibit a kink in $\Delta\tilde{\nu}$ corresponding to their respective kinks in (b). (d) Density distribution of κ_{ref} values for the rot band from RFM. This shows a kink at $\kappa_{ref}^{kink} \approx 40\,m^2\,kg^{-1}$, above which the occurrence of more strongly absorbing wavenumbers declines. The density distribution is computed with respect to $\ln\kappa_{ref}$, in which the bins are equally spaced. (e) Effective emitting width $\Delta\tilde{\nu}$ plotted as a function of $D(p/p_{ref})$WVP, where the vertical axis is exactly inverted relative to that in (d). When plotted this way, the effective emitting width profile mimics the κ_{ref} density, as expected. The gray dotted line in all panels is the tropopause, which lies roughly 100 hPa, ~3.5 km, above the RFM kink.

the rot band for BASE in Fig. 5a. From this plot it is not obvious why $\mathscr{H}$ exhibits a kink at roughly 250 hPa, with a sharp decrease above; to the contrary, the characteristic value of $\partial_p \mathscr{T}_{\tilde{\nu}}$ actually *increases* with height, in accordance with Eq. (8).

Of course, $\mathscr{H}$ involves a spectral integral, so we consider instead the *integrated* transmissivity gradient:

$$\overline{\partial_p \mathscr{T}_{\tilde{\nu}}} \equiv \int_{10\mathrm{cm}^{-1}}^{1000\mathrm{cm}^{-1}} d\tilde{\nu}\, \partial_p \mathscr{T}_{\tilde{\nu}}. \tag{19}$$

Figure 5b confirms that this quantity does indeed exhibit a kink at the right height, and that this feature is reproduced by the SSM2D. Since transmissivity gradients can also be interpreted as emissivity-to-space gradients (section 4), this upper-tropospheric kink in $\overline{\partial_p \mathscr{T}_{\tilde{\nu}}}$ can also be thought of as a precise quantification of the "declining water vapor emissivity" referred to in the FAT literature (Hartmann and Larson 2002; Hartmann et al. 2001). Also, the kink in $\overline{\partial_p \mathscr{T}_{\tilde{\nu}}}$ tells us that additional variations in $B(\tilde{\nu}, T)$ are not required to produce the kink in $\mathscr{H}_{rot}$: if $B(\tilde{\nu}, T)$ were a constant function, $\mathscr{H}_{rot}$ would be proportional to $\overline{\partial_p \mathscr{T}_{\tilde{\nu}}}$ [by Eq. (5)] and hence would still exhibit a kink, without variations in $B(\tilde{\nu}, T)$.

We may thus conclude that the kink in $\mathscr{H}$ stems from the kink in $\overline{\partial_p \mathscr{T}_{\tilde{\nu}}}$. But what, then, causes the kink in $\overline{\partial_p \mathscr{T}_{\tilde{\nu}}}$? Since the integrand in Eq. (19) is not decreasing with height, a plausible alternative hypothesis is that the kink is due to changes in the spectral width over which $\partial_p \mathscr{T}_{\tilde{\nu}}$ is significant, that is, changes in the effective emitting width $\Delta\tilde{\nu}$. We quantified this earlier in section 4 as a constant $\Delta\tilde{\nu} = l_j e$ for the SSM1D, but now generalize it for application to RFM and the SSM2D as simply the range of wavenumbers for which $e^{-e/2} < \tau_{\tilde{\nu}} < e^{e/2}$:

$$\Delta\tilde{\nu} \equiv \int_{10\text{cm}^{-1}}^{1000\text{cm}^{-1}} d\tilde{\nu}\, H(\tau_{\tilde{\nu}} - e^{-e/2}) H(e^{e/2} - \tau_{\tilde{\nu}}). \quad (20)$$

Here H is the Heaviside step function, and the range of $\tau_{\tilde{\nu}}$ values is chosen such that $\Delta\tilde{\nu}$ indeed yields the SSM1D value of $l_{\text{rot}}e \approx 165\,\text{cm}^{-1}$ almost everywhere when calculated for the SSM2D using Eq. (12).[12] Profiles of $\Delta\tilde{\nu}$ for RFM, SSM2D, and SSM1D are shown in Fig. 5c. Both RFM and SSM2D exhibit a kink in their $\Delta\tilde{\nu}$ profiles at the same height at which their respective $\mathscr{H}$ kinks occur. This is consistent with the hypothesis that the kink is caused by a decline in integrated transmissivity gradient $\overline{\partial_p \mathscr{T}_{\tilde{\nu}}}$, which itself is caused by a decline in effective emitting width $\Delta\tilde{\nu}$.[13]

What about the kink in Fig. 3 in the SSM1D $\mathscr{H}$ profile? In the SSM1D [Eq. (17)], $\overline{\partial_p \mathscr{T}_{\tilde{\nu}}} = \beta_{\text{H}_2\text{O}} l_{\text{rot}}/p$ and $\Delta\tilde{\nu} = l_{\text{rot}}e$, both of which match the SSM2D in the lower troposphere but neither of which features a kink (Figs. 5b and 5c, solid red line). According to Eq. (16), then, the kink in the SSM1D $\mathscr{H}$ profile in Fig. 3 must then stem from an upper-tropospheric decline in $\pi B(\tilde{\nu}_{1,\text{rot}}, T)$, which as we argued above is not necessary for a kink in the SSM2D or in RFM. This suggests that the SSM1D, by not allowing $\Delta\tilde{\nu}$ to vary, is too simple to accurately model the kink in $\mathscr{H}$. Note also that gray models, for which $\Delta\tilde{\nu}$ is not even defined, are also too simple to accurately model the kink in $\mathscr{H}$.

Although the $\Delta\tilde{\nu}$ diagnostic is intuitive, it is derived from the $\tau_{\tilde{\nu}}$ field and thus convolves spectroscopy with thermodynamic profiles. Is it possible to think of the $\mathscr{H}_{\tilde{\nu}}$ kink in purely spectroscopic terms? The distribution of κ_{ref} values from RFM for the rot band is shown in Fig. 5d, and indeed one finds a kink there at

$$\kappa_{\text{ref}}^{\text{kink}} \equiv 40\,\text{m}^2\,\text{kg}^{-1} \quad (21)$$

[note that the value of $\kappa_{\text{ref}}^{\text{kink}}$ depends on the p_{ref} at which absorption coefficients are evaluated; cf. Eq. (3)]. Above this preferred value, there is a sharp decline in the occurrence of more strongly absorbing wavenumbers. This is also roughly consistent with Figs. 2a and 2d, in which the (bin averaged and parameterized, respectively) spectral κ_{ref} distributions peak at roughly $100\,\text{m}^2\,\text{kg}^{-1}$.

Is this kink in the κ_{ref} distribution at $\kappa_{\text{ref}}^{\text{kink}}$ causing the kink in $\Delta\tilde{\nu}$ (and hence $\overline{\partial_p \mathscr{T}_{\tilde{\nu}}}$ and $\mathscr{H}_{\tilde{\nu}}$)? If so, then by setting $\tau_{\tilde{\nu}} = 1$ in Eq. (12) we would expect the kink in $\Delta\tilde{\nu}$ to occur where

$$D\frac{p}{p_{\text{ref}}}\text{WVP} \approx \frac{1}{\kappa_{\text{ref}}^{\text{kink}}}. \quad (22)$$

Substituting $p = p_{\text{ref}}(T/T_{\text{ref}})^{g/R_d\Gamma}$ into Eq. (22) and employing the Lambert W function [which satisfies $W(xe^x) = x$] allows us to solve Eq. (22) for the kink temperature T_{kink}:

$$T_{\text{kink}} = \frac{T^*}{W\left[\frac{T^*}{T_{\text{ref}}}(D\,\text{WVP}_0\kappa_{\text{ref}}^{\text{kink}})^{R_d\Gamma/g}\right]} = 214\,\text{K}, \quad (23)$$

where $T^* \equiv (LR_d\Gamma)/(gR_v)$. This agrees reasonably well with the values for T_{kink} given in the literature, solidifying the connection between the kink in the κ_{ref} distribution and that in $\Delta\tilde{\nu}$. Moreover, Eq. (23) helps answer question 2 from the introduction by providing a quantitative, theoretical expression for T_{kink} in terms of only fundamental constants, basic atmospheric parameters (such as RH and Γ), and the preferred value $\kappa_{\text{ref}}^{\text{kink}}$ of H_2O absorption coefficient.

To further check the picture that led to Eq. (23), we plot $\Delta\tilde{\nu}$ versus $D(p/p_{\text{ref}})\text{WVP}$ in Fig. 5e. This profile indeed exhibits a kink near $D(p/p_{\text{ref}})\text{WVP} = 1/\kappa_{\text{ref}}^{\text{kink}} = 0.025\,\text{kg}\,\text{m}^{-2}$, as expected from Eq. (22). Furthermore, the whole shape of the $\Delta\tilde{\nu}$ profile when plotted this way mimics the shape of the κ_{ref} distribution in Fig. 5d, as it should: κ_{ref} values that occur more frequently should give rise to corresponding peaks in $\Delta\tilde{\nu}$, and this correspondence is made plain by plotting $\Delta\tilde{\nu}$ using $D(p/p_{\text{ref}})\text{WVP}$ as the vertical coordinate.

To summarize, the kink in the heating rate $\mathscr{H}$ is due to a kink in $\overline{\partial_p \mathscr{T}_{\tilde{\nu}}}$, which stems from a kink in $\Delta\tilde{\nu}$. The latter arises from a kink in the κ_{ref} distribution. Thus, the $\mathscr{H}$ kink ultimately has a spectroscopic origin. By Eq. (22), however, the kink in the κ_{ref} distribution implies that the kink in $\mathscr{H}$ must occur at a preferred value of $D(p/p_{\text{ref}})\text{WVP}$, yielding the characteristic kink temperature Eq. (23). This kink temperature is strongly influenced by the CC scaling of WVP [Eq. (11)], roughly consistent with the broader FAT hypothesis that radiative cooling declines at a fixed temperature due to the CC scaling of water vapor pressure. However, Eq. (22) shows that other physics is also relevant, in particular the preferred value $\kappa_{\text{ref}}^{\text{kink}}$ of H_2O absorption coefficient (which is required for CC scaling to determine a preferred temperature), along with a minor modification from pressure broadening.

[12] To derive this range, note that over a spectral range of width $\Delta\tilde{\nu} = l_{\text{rot}}e$, $\kappa_{\text{H}_2\text{O}}$ varies by a factor of e^{-e} by Eq. (10). This variation in $\kappa_{\text{H}_2\text{O}}$ leads to variation of $\tau_{\tilde{\nu}}$ between $e^{e/2}$ and $e^{-e/2}$, if the variation is centered geometrically around $\tau_{\tilde{\nu}} = 1$.

[13] It should be noted that the agreement in the troposphere between the RFM and SSM2D profiles in Figs. 5b and 5c benefits to some degree from compensation between the SSM2D's neglect of wavenumbers below $\tilde{\nu}_{\text{rot}} = 150\,\text{cm}^{-1}$ and its enhancement of bin-averaged $\partial_p \mathscr{T}_{\tilde{\nu}}$ (and hence $\mathscr{H}_{\tilde{\nu}}$; Figs. 2c and 2f) due to its neglect of finescale structure. These errors do not affect the conclusion, however, that both RFM and the SSM2D exhibit kinks associated with a decline in $\Delta\tilde{\nu}$.

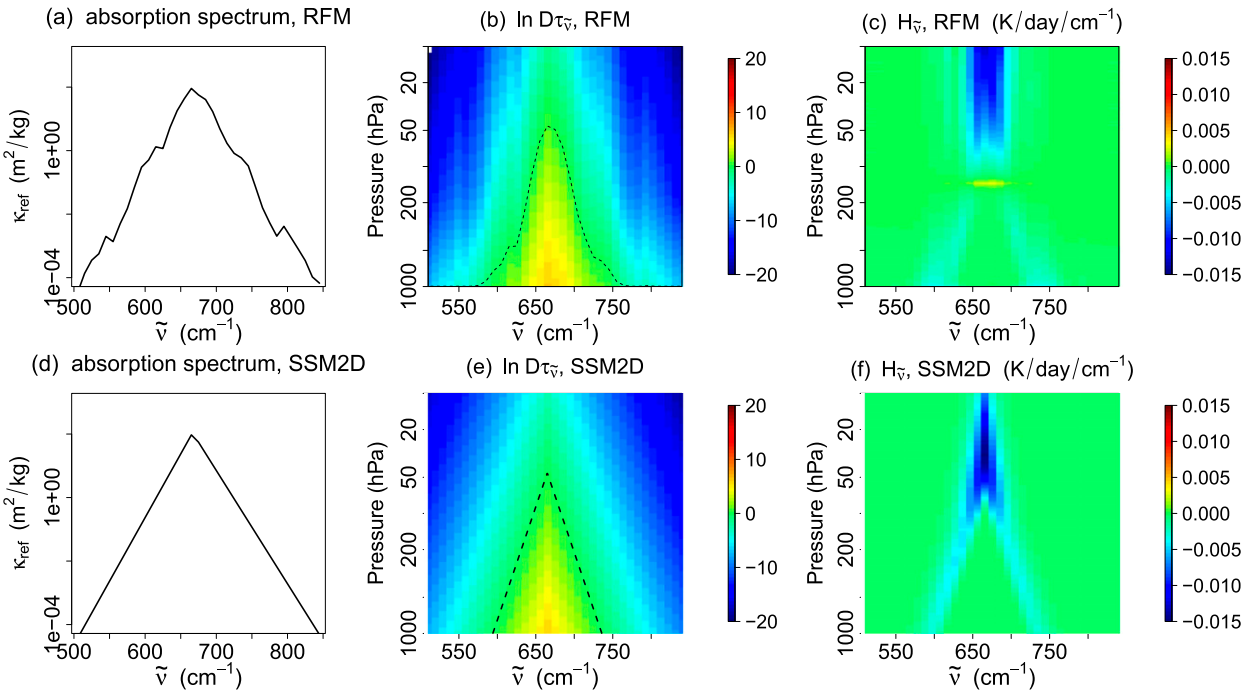

FIG. 6. As in Fig. 2, but for the 500–850-cm^{-1} CO_2 band. (c),(f) The SSM2D again emulates the behavior of RFM, and in particular reproduces the stratospheric enhancement of $\mathscr{H}_{\tilde{\nu}}$.

7. CO_2

Having addressed questions 1 and 2 from the introduction, we now turn to question 3 concerning the stratospheric enhancement of CO_2 cooling rates. Addressing this question requires applying our formalism to CO_2, which we do now.

For CO_2 cooling we run RFM just as described in section 2a, except our $\tilde{\nu}$ range is now 500–850 cm^{-1}, we use a preindustrial CO_2 concentration of 280 ppmv, and RFM's χ factor (from Cousin et al. 1985) is used to suppress far-wing absorption of CO_2. In analogy to Eq. (9), we begin by defining bands for CO_2:

$$\begin{aligned} &CO_2\ P \text{ band: } 500 < \tilde{\nu} < \tilde{\nu}_Q \equiv 667.5\,\mathrm{cm}^{-1} \\ &CO_2\ R \text{ band: } \tilde{\nu}_Q < \tilde{\nu} < 850\,\mathrm{cm}^{-1}, \end{aligned} \tag{24}$$

(here $\tilde{\nu}_Q$ denotes the spectral location of the main CO_2 Q branch, which lies between its associated P and R branches; Coakley and Yang 2014).[14] This band structure can be seen in $\kappa_{\mathrm{ref}}(\tilde{\nu})$ from RFM (Fig. 6a). We then again coarse grain $\ln\kappa_{\mathrm{ref}}(\tilde{\nu})$ over spectral intervals of 10 cm^{-1} and apply a linear fit to $\ln\kappa_{\mathrm{ref}}(\tilde{\nu})$ within each band. These two linear fits give very similar slopes and maxima, so we combine the two fits into a single expression for simplified reference absorption coefficients:

$$\kappa_{CO_2}(\tilde{\nu}) \equiv \kappa_Q \exp\left(-\frac{|\tilde{\nu}-\tilde{\nu}_Q|}{l_Q}\right) \quad \text{for} \quad \tilde{\nu} \text{ in } P \text{ or } R, \tag{25}$$

where $\ln\kappa_Q$ and l_Q are averages of the maxima and slopes from the P and R bands. These parameter values are also tabulated in Table 1. Note that CO_2's l_Q parameter is much smaller than that for H_2O, a point to which we return below.

Next, we obtain expressions for CO_2 optical depth. Evaluating Eq. (2) with pressure broadening (but no temperature scaling) and constant CO_2 specific concentration q (rather than variable q_v) yields

$$\tau_{\tilde{\nu}} = \kappa_{CO_2}(\tilde{\nu})\frac{qp^2}{2gp_{\mathrm{ref}}}. \tag{26}$$

Note that Eqs. (26) and (6) imply

$$\beta_{CO_2} = 2,$$

a value 2–3 times smaller than that for H_2O, because CO_2 is well mixed while H_2O exhibits Clausius–Clapeyron scaling [cf. Eq. (13)].

[14] Spectroscopically speaking, the P and R branches only encompass lines within roughly 30 cm^{-1} of the Q branch, but for simplicity we use P and R to refer to all wavenumbers lower or higher than $\tilde{\nu}_Q$ throughout the 500–850 cm^{-1} spectral interval.

We can now substitute Eq. (26) into Eq. (5) to obtain a spectrally simplified $\mathscr{H}_{\tilde{\nu}}$. This, along with the expressions (25) and (26), constitute the SSM2D for CO_2. These fields, along with their RFM counterparts, are shown in Fig. 6. As with H_2O, the SSM2D captures the broad characteristics of the $\mathscr{H}_{\tilde{\nu}}$ produced by RFM, though again without fine-scale structure.

In particular, the SSM2D reproduces the stratospheric enhancement of $\mathscr{H}_{\tilde{\nu}}$ exhibited by RFM (Figs. 6c,f). From Eqs. (5) and (7) with $\beta_{CO_2} = 2$ we see that this high-altitude enhancement of $\mathscr{H}_{\tilde{\nu}}$ stems from the high-altitude enhancement of β/p. But, what is the meaning of this β/p factor? We know that $\beta/p = (d\tau_{\tilde{\nu}}/dp)|_{\tau_{\tilde{\nu}}=1}$, but why is this optical depth gradient enhanced at low p? To understand this, note that by Eq. (2) we have $(d\tau_{\tilde{\nu}}/dp) = \kappa(\tilde{\nu}, T, p)q/g$. If we set $\tau_{\tilde{\nu}} = 1$ in Eq. (26), and solve for the (absolute, not reference) absorption coefficient κ_1 emitting at a given p, we find

$$\kappa_1 = \frac{2g}{qp}. \tag{27}$$

This is again an inverse relationship between pathlength and absorption coefficient [similar to Eq. (22) for H_2O], and says that the "effective absorption coefficient" κ_1 scales as $1/p$. This $1/p$ scaling is confirmed in Fig. 7, which plots Eq. (27) as well as κ_1 diagnosed directly from RFM by averaging the absolute absorption coefficients at each height over the same wavenumbers contributing to $\Delta\tilde{\nu}$ in Eq. (20). Physically, $\mathscr{H}_{\tilde{\nu}}|_{\tau_{\tilde{\nu}}=1}$ is enhanced at low p because wavenumbers with such strong κ can cool a unit mass of air at a much higher rate than the more weakly absorbing wavenumbers that reach $\tau_{\tilde{\nu}} = 1$ at higher p. This explanation differs from some previously proposed, such as those based on decreased pressure broadening (Petty 2006, p. 317) or H_2O–CO_2 overlap (Zhu et al. 1992).

We are now also in a position to explain why tropospheric CO_2 cooling rates are negligible compared to H_2O. We noted above that β_{CO_2} is 2–3 times smaller than β_{H_2O}, which by Eqs. (5)–(7) tells us that tropospheric $\mathscr{H}_{\tilde{\nu}}$ will also be 2–3 times smaller for CO_2 (cf. Figs. 2 and 6). In other words, because CO_2 optical depth does not increase with pressure as fast as H_2O, its cooling at any given wavenumber is more spread out in the vertical and is thus smaller.[15] This decrease in $\mathscr{H}_{\tilde{\nu}}$ is compounded by CO_2's smaller effective emitting width $\Delta\tilde{\nu}$, which is roughly $l_Q e \approx 35\,\mathrm{cm}^{-1}$, approximately 1/5 that of H_2O (cf. Figs. 2 and 6). Together, these two effects imply that spectrally integrated radiative cooling $\mathscr{H}$ from CO_2 will only be a fraction of that from H_2O.[16] Due to its relative insignificance in the troposphere, then, we resist the temptation to construct an SSM1D for CO_2, though it is straightforward from here.

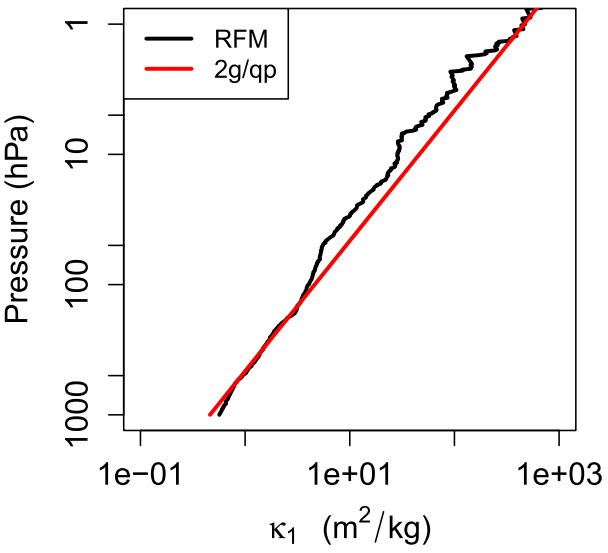

FIG. 7. Profiles of the effective absorption coefficient κ_1 for CO_2, as predicted by Eq. (27) (red) as well as diagnosed from RFM (black) by linearly averaging $\kappa(\tilde{\nu}, p)$ over those $\tilde{\nu}$ that also contribute to $\Delta\tilde{\nu}$ in Eq. (20). The good agreement confirms the $1/p$ scaling for κ_1, which underlies the stratospheric enhancement of $\mathscr{H}_{\tilde{\nu}}$ (Fig. 6).

8. Summary and discussion

Our main results can be summarized as follows:

- The characteristic $\mathscr{H}$ value of $-2 \pm 0.5\,\mathrm{K\,day}^{-1}$ can be obtained as the product of the Planck function, a vertical emissivity gradient, and an effective emitting width, all of which can be estimated via the SSM1D [Eq. (18)]. This characteristic value is relatively insensitive to typical RH and Γ variations, but is sensitive to T_s (Fig. 4).
- The upper-tropospheric kink in $\mathscr{H}$ ultimately stems from a kink in the distribution of absorption coefficients κ_{ref} in the H_2O rot band (Fig. 5). The value of κ_{ref} at this kink determines T_{kink} via Eq. (23).
- The stratospheric enhancement of CO_2 cooling is due to the $1/p$ factor in the transmissivity gradient in Eq. (7). This $1/p$ factor itself can be traced to the strength of the effective absorption coefficients that emit from a given height [Eq. (27) and Fig. 7].

[15] This also has implications for the validity of the CTS approximation for CO_2, as discussed in Jeevanjee and Fueglistaler (2020).

[16] This story is of course reversed in the stratosphere, where CO_2 cooling dominates over that from H_2O (Manabe et al. 1964) even though both gases are well mixed and have $\beta = 2$. This is likely due to the relatively low concentration of water vapor in the stratosphere (23 ppmv here vs 280 ppmv of CO_2), which yields low-stratospheric WVP values and hence low $\Delta\tilde{\nu}$ values (cf. Figs. 5c,e).

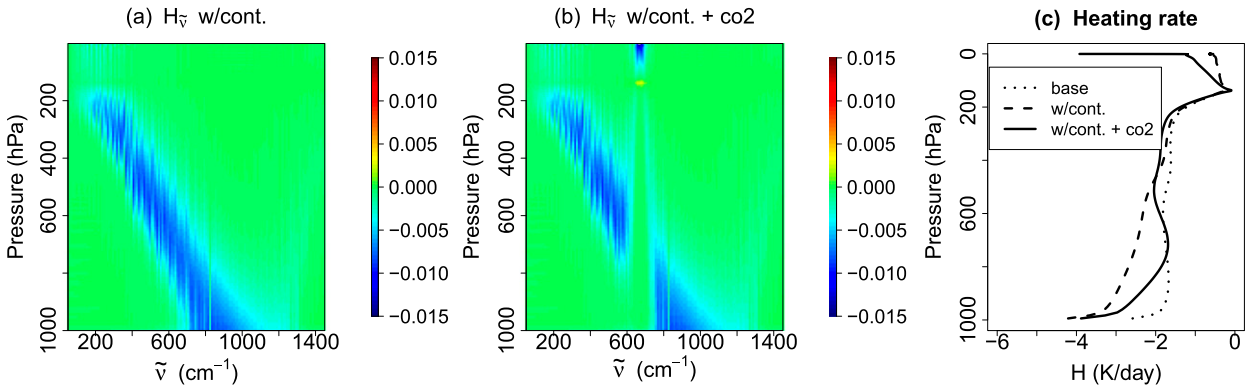

FIG. A1. Spectrally resolved radiative cooling $\mathscr{H}_{\tilde{\nu}}$ as output from RFM for the BASE atmosphere with (a) the H_2O continuum included and (b) H_2O continuum plus CO_2 absorption. (c) The spectrally integrated cooling rates $\mathscr{H}$ for these cases plus BASE. Continuum emission enhances $\mathscr{H}$, particularly in the lower troposphere, but this effect is largely canceled out by CO_2 absorption.

This work could be generalized and extended in various ways. One extension would be to use the SSM1D, which by providing $\tau_{\tilde{\nu}} = 1$ contours identifies an emission height for each wavenumber $\tilde{\nu}$, to generate an estimate for spectrally resolved OLR. A first attempt at this for H_2O only, without the continuum, is given in appendix C and Fig. C1. Further work could incorporate idealized models of H_2O–CO_2 overlap, as well as the H_2O continuum, for estimation of both $\mathscr{H}$ and OLR. One could also formulate a simplified spectroscopy akin to Eqs. (10) and (25) for other important greenhouse gases such as methane and ozone, and thus incorporate those gases into the SSMs.

Another direction for future work would be to investigate the radiative cooling profiles of less idealized atmospheres, and in particular atmospheres with nonuniform RH profiles, as nonuniform RH can significantly affect radiative cooling. For example, Seeley et al. (2019b) found that the kink disappeared in cloud-resolving radiative–convective equilibrium simulations at T_s of 270 K and colder, but further investigation showed that the kink reappeared when the simulated RH profiles were replaced with a uniform RH profile (not shown). Observations of nonuniform RH profiles are discussed in Stevens et al. (2017), who focused on strong vertical RH gradients observed in the subtropics and emphasized the implications of these RH gradients for radiative cooling profiles and the associated circulations. Similar effects have also been studied in the context of radiative instabilities and self-aggregation of convection (Beucler et al. 2018; Beucler and Cronin 2016; Emanuel et al. 2014).

While the primary goal of this work was to shed light on questions 1–3 posed in the introduction, an ancillary benefit was the development of the SSMs, which might be thought of as filling in the intermediate rungs of a "radiation hierarchy," with gray models on the bottom rung and line-by-line codes like RFM at the top. Moving between these rungs to generate and test hypotheses exemplifies the "hierarchical" approach to climate science (Maher et al. 2019; Jeevanjee et al. 2017; Polvani et al. 2017; Held 2005; Hoskins 1983; Schneider and Dickinson 1974).

The intermediate complexity SSMs could also be used to augment or replace gray models where they are still used for research purposes, as the distortions of the gray approximation evident in Fig. 1b suggest that inferences drawn from gray radiation models, as well as fluid-dynamical models coupled to them, may not be reliable (e.g., Tan et al. 2019). As another example of inaccuracies of the gray approximation, the gray model in Fig. 1b, which was tuned to exhibit the same 170 W m^{-2} column-integrated cooling as RFM, also yields an OLR of 170 W m^{-2}, which is a serious underestimate[17] of RFM's OLR value of 325 W m^{-2}. Despite such errors, however, gray models are still in use in both astronomy (e.g., Parmentier and Guillot 2014; Rauscher and Menou 2012; Robinson and Catling 2012; Heng et al. 2011) as well as terrestrial atmospheric sciences, both for understanding (Hu and Vallis 2019; Goessling and Bathiany 2016; Vallis et al. 2015) and also as radiation schemes for idealized aquaplanet models (e.g., Frierson et al. 2006; see Maher et al. 2019) and Jeevanjee et al. (2017) for extensive further references]. The SSMs could prove useful as alternative, cheap, clear-sky radiation schemes that still only depend on a few parameters (cf. Table 1) but are nonetheless spectral and avoid the distortions of the gray approximation.

Acknowledgments. We thank ECMWF for providing the ERA-Interim data. This research was supported by NSF Grants AGS-1417659 and AGS-1660538, and NJ

[17] This error can be addressed by introducing a spectral "window" to the gray model (e.g., Weaver and Ramanathan 1995), but such "window gray" models still suffer from the unrealistic cooling profiles of Fig. 1b.

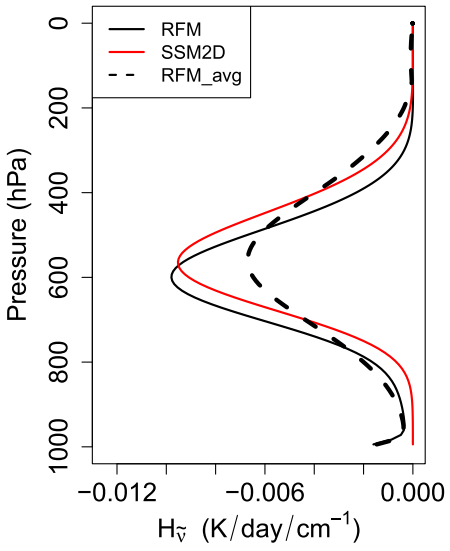

FIG. B1. Spectrally resolved radiative cooling profiles $\mathscr{H}_{\tilde{\nu}}(p)$ for BASE from both RFM (black line) and SSM2D (red line) at $\tilde{\nu} = 508.6$ and $\tilde{\nu} = 505\,\mathrm{cm}^{-1}$, respectively, where both models have $\kappa_{\mathrm{ref}} = 0.125\,\mathrm{m}^2\,\mathrm{kg}^{-1}$. Despite small errors, the SSM2D profile captures the shape, amplitude, and position of the RFM profile, validating the SSM2D. The dashed line shows the average of such RFM profiles across a 10-cm^{-1}-wide bin centered on 508.6 cm^{-1}. This coarse graining yields a "smeared out" profile that is broader and has smaller amplitude, consistent with Fig. 2c. The vertical integrals of all three profiles in this plot agree to within 5%.

was supported by a Hess Fellowship from the Princeton Geosciences department. NJ thanks David Romps for guidance in early stages of this work and for suggesting the delta function approach to integrating Eq. (15). NJ also thanks Jacob Seeley and Robert Pincus for discussions, feedback, and encouragement, as well as Dennis Hartmann and two anonymous reviewers for very helpful and detailed reviews. RFM output and R scripts used in producing this manuscript are available (at https://github.com/jeevanje/17rad_cooling2.git).

APPENDIX A

Sensitivity to H_2O Continuum and CO_2 Overlap

The RFM calculations in the main text neglected the water vapor continuum as well as overlap effects between H_2O and CO_2, both of which are known to affect radiative cooling and OLR. While we do not pursue simple models of these effects, this appendix investigates the errors induced by neglecting them, and discusses why our 1D RFM calculation that neglects these effects nonetheless resembles the ECMWF profile in Fig. 1b, which includes them.

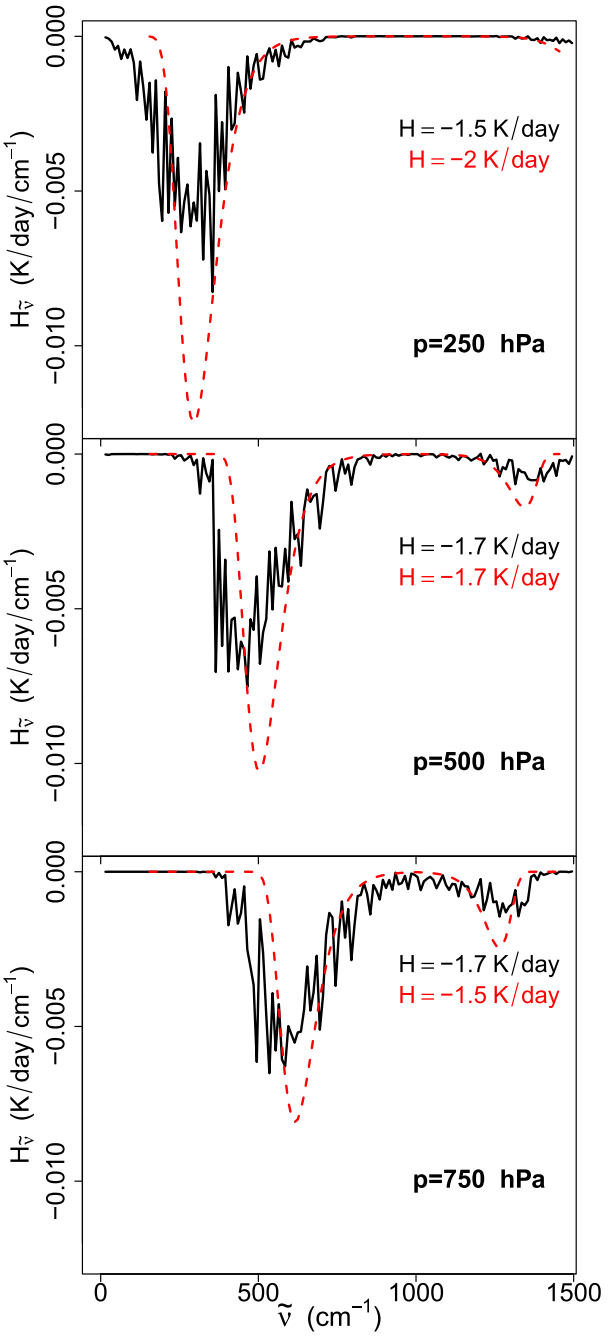

FIG. B2. Spectrally resolved cooling distribution $\mathscr{H}_{\tilde{\nu}}(\tilde{\nu})$ for BASE at $p = 250$, 500, and 750 hPa, from RFM (black solid lines) and SSM2D (red dashed line), where the RFM output is averaged over bins of width 10 cm^{-1}. As for the vertical profiles in Fig. B1, the coarse graining of RFM output yields a cooling distribution that is broader and of smaller amplitude than the corresponding SSM2D distribution. Again, however, the spectral integrals are comparable, though with errors somewhat larger than for the vertical integrals in Fig. B1. See text for discussion.

We first consider the H_2O continuum. Figure A1a shows $\mathscr{H}_{\tilde{\nu}}$ from an RFM calculation identical to BASE, but with the continuum turned on (RFM uses the MT_CKD continuum; Mlawer et al. 2012). The spectrally integrated $\mathscr{H}$ profile from this case is shown in Fig. A1c. The continuum increases $\mathscr{H}$ throughout the troposphere, especially at lower levels. When we then add on the effects of CO_2 overlap (Figs. A1b,c), however, we find that much of this increase is cancelled due to the presence of CO_2. From Fig. A1c we see that the only real contrast between our base case and the more realistic case with both continuum and CO_2 contributions is for pressures greater than 850 hPa or so, corresponding to temperatures of 290 K or above (thinking here in temperature coordinates). Such temperatures may not necessarily make a strong contribution to the globally averaged $\mathscr{H}$ profile shown in Fig. 1, which is averaged on pressure levels and thus conflates different temperatures.

APPENDIX B

Further Validation of the SSM2D

Toward the end of section 3a we discussed a discrepancy between coarse-grained RFM $\mathscr{H}_{\tilde{\nu}}$ and that produced by the SSM2D, namely that the RFM $\mathscr{H}_{\tilde{\nu}}$ field appears "smeared out" relative to the SSM2D $\mathscr{H}_{\tilde{\nu}}$ field (Figs. 2c,f). The purpose of this appendix is to demonstrate that this error does not occur at individual wavenumbers, but occurs as a result of finescale spectral structure and the resulting coarse graining we impose for clarity.

Figure B1 shows profiles of $\mathscr{H}_{\tilde{\nu}}$ from both RFM and SSM2D at $\tilde{\nu} = 508.6$ and $\tilde{\nu} = 505\,\mathrm{cm}^{-1}$, respectively, where both models have $\kappa_{\mathrm{ref}} = 0.125\,\mathrm{m}^2\,\mathrm{kg}^{-1}$. Apart from a small offset due to our neglect of temperature scaling, as well as a lack of cooling near the surface due to the CTS approximation (Jeevanjee and Fueglistaler 2020), the SSM2D captures the shape, amplitude, and position of the RFM $\mathscr{H}_{\tilde{\nu}}$ profile quite well. In Fig. 2c, however, what is plotted are $\mathscr{H}_{\tilde{\nu}}$ profiles averaged across 10-cm^{-1} bins. Due to the marked finescale structure in $\kappa_{\mathrm{ref}}(\tilde{\nu})$, within each bin we are thus averaging $\mathscr{H}_{\tilde{\nu}}$ profiles with a wide variety of κ_{ref} values and thus a wide variety of heights at which they peak. The resulting $\mathscr{H}_{\tilde{\nu}}$ profile for the relevant RFM bin is shown in the dashed curve of Fig. B1, and is indeed smeared out relative to the RFM and SSM2D $\mathscr{H}_{\tilde{\nu}}$ profiles at a single wavenumber. This averaging should not degrade the column integrals of $\mathscr{H}_{\tilde{\nu}}$, however, and calculating those indeed yields agreement, to within 5% (not shown).

What about $\mathscr{H}_{\tilde{\nu}}$ as a function of $\tilde{\nu}$, rather than pressure? These are plotted for both RFM and SSM2D in Fig. B2. Here, since we are plotting $\mathscr{H}_{\tilde{\nu}}$ as a function of wavenumber, we apply our coarse graining for clarity, and thus the RFM profiles are again smeared out relative to the SSM profile, analogous to what is seen in Fig. B1. Again, however, the integrals (now spectral rather than column) largely agree, though at times with larger errors, up to 25%. These errors seem to be related to the fact that our narrowly peaked $\mathscr{H}_{\tilde{\nu}}(\tilde{\nu})$ profiles sample the Planck function $B(\tilde{\nu}, T)$ over a narrow spectral range, whereas the RFM $\mathscr{H}_{\tilde{\nu}}$ profiles sample $B(\tilde{\nu}, T)$ over a significantly larger range, over which nonlinearity of the Planck function becomes significant.

APPENDIX C

SSM OLR

The formalism developed here can also be applied to estimate the spectrally resolved outgoing longwave radiation $\mathrm{OLR}_{\tilde{\nu}} \equiv F_{\tilde{\nu}}(p = 0)$, where we estimate this as simply the Planck function evaluated at an effective emission temperature $T_1(\tilde{\nu})$. We estimate this by setting $\tau_{\tilde{\nu}} = 1$ in Eq. (12) and solving for T; this is essentially the same calculation we performed to obtain Eq. (23), except in this case we leave $\kappa_{\mathrm{ref}}(\tilde{\nu})$ unspecified, yielding

$$T_1(\tilde{\nu}) = \frac{T^*}{W\left\{\frac{T^*}{T_{\mathrm{ref}}}[D\,\mathrm{WVP}_0\kappa_{\mathrm{ref}}(\tilde{\nu})]^{R_d\Gamma/g}\right\}}. \tag{C1}$$

For some $\tilde{\nu}$, however, $T_1(\tilde{\nu})$ will be undefined because $\tau_{\tilde{\nu}} < 1$ even at the surface; this is the water vapor "window" region $\tilde{\nu}_{1,\mathrm{rot}}(T_s) < \tilde{\nu} < \tilde{\nu}_{1,\mathrm{v-r}}(T_s)$, for which we set $\mathrm{OLR}_{\tilde{\nu}}$ equal to surface Planck emission. Mathematically, our estimate for $\mathrm{OLR}_{\tilde{\nu}}$ is then

$$\mathrm{OLR}_{\tilde{\nu}} = \begin{cases} \pi B[\tilde{\nu}, T_1(\tilde{\nu})] & \text{where} \quad T_1(\tilde{\nu}) \text{ is defined} \\ \pi B(\tilde{\nu}, T_s) & \text{where} \quad \tilde{\nu}_{1,\mathrm{rot}}(T_s) < \tilde{\nu} < \tilde{\nu}_{1,\mathrm{v\text{-}r}}(T_s) \quad \text{(window region)} \end{cases}. \tag{C2}$$

We refer to Eqs. (C1) and (C2) as the simple spectral model for OLR (SSM OLR).

Figure C1 shows the SSM OLR for our BASE atmosphere, along with $\mathrm{OLR}_{\tilde{\nu}}$ as output directly from RFM.

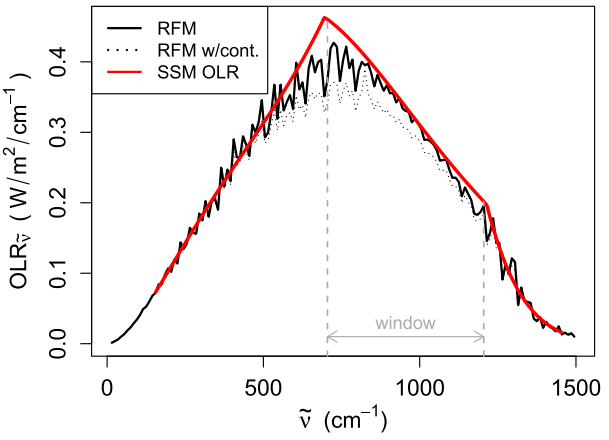

FIG. C1 . Spectrally resolved outgoing longwave radiation $\mathrm{OLR}_{\tilde{\nu}}$ from H_2O only, as computed from RFM (black line) and SSM OLR (red line). The SSM OLR captures the shape of RFM's $\mathrm{OLR}_{\tilde{\nu}}$, and also shows that the peak in $\mathrm{OLR}_{\tilde{\nu}}$ is due to the onset of the water vapor window. This conclusion is unchanged by comparing to RFM's $\mathrm{OLR}_{\tilde{\nu}}$ computed with the H_2O continuum (dotted line).

The SSM OLR, while crude, quantitatively captures the gross spectral shape of RFM's $\mathrm{OLR}_{\tilde{\nu}}$ quite well. Furthermore, it gives us some insight into this shape, as follows. Both the RFM and SSM OLR curves peak at the beginning of the window region, $\tilde{\nu}_{1,\mathrm{rot}}(T_s) \approx 750\,\mathrm{cm}^{-1}$, and the SSM OLR curve in particular has a cusp. This is because beyond $\tilde{\nu}_{1,\mathrm{rot}}(T_s)$, the emission temperature is no longer increasing with $\tilde{\nu}$ but rather becomes constant at T_s, allowing the explicit $\tilde{\nu}$ dependence of $B(\tilde{\nu}, T)$ to take over and cause an immediate and sharp decline in $\mathrm{OLR}_{\tilde{\nu}}$. Thus the peak in $\mathrm{OLR}_{\tilde{\nu}}$ is caused by a temperature-driven increase for $\tilde{\nu} < \tilde{\nu}_{1,\mathrm{rot}}(T_s)$ and a $\tilde{\nu}$-driven decrease for $\tilde{\nu} > \tilde{\nu}_{1,\mathrm{rot}}(T_s)$. Adding the H_2O continuum to our RFM calculation does not change this picture (Fig. C1, dotted line). This peak is typically obscured in more realistic calculations by the strong 667 cm^{-1} CO_2 absorption feature, but understanding the H_2O-only case seems like a prerequisite for understanding these more realistic cases, which could be pursued along similar lines.

REFERENCES

Beucler, T., and T. W. Cronin, 2016: Moisture-radiative cooling instability. *J. Adv. Model. Earth Syst.*, **8**, 1620–1640, https://doi.org/10.1002/2016ms000763.

——, ——, and K. Emanuel, 2018: A linear response framework for radiative-convective instability. *J. Adv. Model. Earth Syst.*, **10**, 1924–1951, https://doi.org/10.1029/2018MS001280.

Clough, S. A., M. J. Iacono, and J.-l. Moncet, 1992: Line-by-line calculations of atmospheric fluxes and cooling rates: Application to water vapor. *J. Geophys. Res.*, **97**, 15 761–15 785 https://doi.org/10.1029/92JD01419.

Coakley, J. A., Jr., and P. Yang, 2014: *Atmospheric Radiation: A Primer with Illustrative Solutions*. Wiley, 239 pp.

Costa, S. M. S., and K. P. Shine, 2012: Outgoing longwave radiation due to directly transmitted surface emission. *J. Atmos. Sci.*, **69**, 1865–1870, https://doi.org/10.1175/JAS-D-11-0248.1.

Cousin, C., R. L. Doucen, C. Boulet, and A. Henry, 1985: Temperature dependence of the absorption in the region beyond the 4.3-μm band head of CO_2. 2: N_2 and O_2 broadening. *Appl. Opt.*, **24**, 3899–3907, https://doi.org/10.1364/AO.24.003899.

Dee, D. P., and Coauthors, 2011: The ERA-Interim reanalysis: Configuration and performance of the data assimilation system. *Quart. J. Roy. Meteor. Soc.*, **137**, 553–597, https://doi.org/10.1002/qj.828

Dudhia, A., 2017: The Reference Forward Model (RFM). *J. Quant. Spectrosc. Radiat. Transfer*, **186**, 243–253, https://doi.org/10.1016/J.JQSRT.2016.06.018.

Dufresne, J. L., R. Fournier, C. Hourdin, and F. Hourdin, 2005: Net exchange reformulation of radiative transfer in the CO_2 15-μm band on Mars. *J. Atmos. Sci.*, **62**, 3303–3319, https://doi.org/10.1175/JAS3537.1.

Eitzen, Z. A., K. M. Xu, and T. Wong, 2009: Cloud and radiative characteristics of tropical deep convective systems in extended cloud objects from CERES observations. *J. Climate*, **22**, 5983–6000, https://doi.org/10.1175/2009JCLI3038.1.

Emanuel, K. A., A. A. Wing, and E. M. Vincent, 2014: Radiative-convective instability. *J. Adv. Model. Earth Syst.*, **6**, 75–90, https://doi.org/10.1002/2013MS000270.

Fels, S. B., and M. D. Schwarzkopf, 1975: The simplified exchange approximation: A new method for radiative transfer calculations. *J. Atmos. Sci.*, **32**, 1475–1488, https://doi.org/10.1175/1520-0469(1975)032<1475:tseaan>2.0.co;2.

Frierson, D. M. W., I. M. Held, and P. Zurita-Gotor, 2006: A gray-radiation aquaplanet moist GCM. Part I: Static stability and eddy scale. *J. Atmos. Sci.*, **63**, 2548–2566, https://doi.org/10.1175/JAS3753.1.

Gasiorowicz, S., 2003: *Quantum Physics*. Wiley, 336 pp.

Goessling, H. F., and S. Bathiany, 2016: Why CO_2 cools the middle atmosphere—A consolidating model perspective. *Earth Syst. Dyn.*, **7**, 697–715, https://doi.org/10.5194/esd-7-697-2016.

Green, J. S., 1967: Division of radiative streams into internal transfer and cooling to space. *Quart. J. Roy. Meteor. Soc.*, **93**, 371–372, https://doi.org/10.1002/qj.49709339710.

Harries, J., and Coauthors, 2008: The far-infrared Earth. *Rev. Geophys.*, **46**, RG4004, https://doi.org/10.1029/2007RG000233.

Harrop, B. E., and D. L. Hartmann, 2012: Testing the role of radiation in determining tropical cloud-top temperature. *J. Climate*, **25**, 5731–5747, https://doi.org/10.1175/JCLI-D-11-00445.1.

Hartmann, D. L., and K. Larson, 2002: An important constraint on tropical cloud–climate feedback. *Geophys. Res. Lett.*, **29**, 1951, https://doi.org/10.1029/2002GL015835.

——, J. R. Holton, and Q. Fu, 2001: The heat balance of the tropical tropopause, cirrus, and stratospheric dehydration. *Geophys. Res. Lett.*, **28**, 1969–1972, https://doi.org/10.1029/2000GL012833.

Held, I. M., 2005: The gap between simulation and understanding in climate modeling. *Bull. Amer. Meteor. Soc.*, **86**, 1609–1614, https://doi.org/10.1175/BAMS-86-11-1609.

Heng, K., D. M. W. Frierson, and P. J. Phillipps, 2011: Atmospheric circulation of tidally locked exoplanets: II. Dual-band radiative transfer and convective adjustment. *Mon. Notes Roy. Astron. Soc.*, **418**, 2669–2696, https://doi.org/10.1111/j.1365-2966.2011.19658.x.

Hoskins, B. J., 1983: Dynamical processes in the atmosphere and the use of models. *Quart. J. Roy. Meteor. Soc.*, **109**, 1–21, https://doi.org/10.1002/QJ.49710945902.

Houghton, J. T., 2002: *The Physics of Atmospheres*. Cambridge University Press, 320 pp.

Hu, S., and G. K. Vallis, 2019: Meridional structure and future changes of tropopause height and temperature. *Quart. J. Roy. Meteor. Soc.*, **145**, 2698–2717, https://doi.org/10.1002/QJ.3587.

Jeevanjee, N., 2018: The physics of climate change: Simple models in climate science. arXiv, http://arxiv.org/abs/1802.02695.

——, and S. Fueglistaler, 2020: On the cooling-to-space approximation. *J. Atmos. Sci.*, **77**, 465–478, https://doi.org/10.1175/JAS-D-18-0352.1.

——, P. Hassanzadeh, S. Hill, and A. Sheshadri, 2017: A perspective on climate model hierarchies. *J. Adv. Model. Earth Syst.*, **9**, 1760–1771, https://doi.org/10.1002/2017MS001038.

Joseph, J. M., and R. Bursztyn, 1976: A radiative cooling model in the thermal infrared for application to models of the general circulation. *J. Appl. Meteor.*, **15**, 319–325, https://doi.org/10.1175/1520-0450(1976)015<0319:ARCMIT>2.0.CO;2.

Koll, D. D., and T. W. Cronin, 2018: Earth's outgoing longwave radiation linear due to H_2O greenhouse effect. *Proc. Natl. Acad. Sci. USA*, **115**, 10 293–10 298, https://doi.org/10.1073/pnas.1809868115.

Kuang, Z., and D. L. Hartmann, 2007: Testing the fixed anvil temperature hypothesis in a cloud-resolving model. *J. Climate*, **20**, 2051–2057, https://doi.org/10.1175/JCLI4124.1.

Kubar, T. L., D. L. Hartmann, and R. Wood, 2007: Radiative and convective driving of tropical high clouds. *J. Climate*, **20**, 5510–5526, https://doi.org/10.1175/2007JCLI1628.1.

Li, Y., P. Yang, G. R. North, and A. Dessler, 2012: Test of the fixed anvil temperature hypothesis. *J. Atmos. Sci.*, **69**, 2317–2328, https://doi.org/10.1175/JAS-D-11-0158.1.

Maher, P., and Coauthors, 2019: Model hierarchies for understanding atmospheric circulation. *Rev. Geophys.*, **57**, 250–280, https://doi.org/10.1029/2018RG000607.

Manabe, S., R. F. Strickler, S. Manabe, and R. F. Strickler, 1964: Thermal equilibrium of the atmosphere with a convective adjustment. *J. Atmos. Sci.*, **21**, 361–385, https://doi.org/10.1175/1520-0469(1964)021<0361:TEOTAW>2.0.CO;2.

Mapes, B. E., 2001: Water's two scale heights: The moist adiabat and the radiative troposphere. *Quart. J. Roy. Meteor. Soc.*, **127**, 2353–2366, https://doi.org/10.1002/QJ.49712757708.

Mlawer, E. J., S. J. Taubman, P. D. Brown, M. J. Iacono, and S. A. Clough, 1997: Radiative transfer for inhomogeneous atmospheres: RRTM, a validated correlated-k model for the longwave. *J. Geophys. Res.*, **102**, 16 663–16 682, https://doi.org/10.1029/97JD00237.

——, V. H. Payne, J.-L. Moncet, J. S. Delamere, M. J. Alvarado, and D. C. Tobin, 2012: Development and recent evaluation of the MT_CKD model of continuum absorption. *Philos. Trans. Roy. Soc.*, **370A**, 2520–2556, https://doi.org/10.1098/RSTA.2011.0295.

Morcrette, J.-J., S. A. Clough, E. J. Mlawer, and M. J. Iacono, 1998: Impact of a validated radiative transfer scheme, RRTM, on the ECMWF model climate and 10 day forecasts. ECMWF Tech. Memo. 252, 46 pp., https://www.ecmwf.int/node/11252.

Parmentier, V., and T. Guillot, 2014: A non-grey analytical model for irradiated atmospheres. *Astron. Astrophys.*, **562**, A133, https://doi.org/10.1051/0004-6361/201322342.

Petty, G. W., 2006: *A First Course in Atmospheric Radiation*. 2nd ed. Sundog Publishing, 472 pp.

Pierrehumbert, R. T., 2010: *Principles of Planetary Climate*. Cambridge University Press, 635 pp.

Polvani, L., B. Medeiros I. Simpson, A. Clement, and J. Benedict, 2017: When less is more: Opening the door to simpler climate models. *Eos, Trans. Amer. Geophys. Union*, **98**, https://doi.org/10.1029/2017EO079417.

Rauscher, E., and K. Menou, 2012: A general circulation model for gaseous exoplanets with double-gray radiative transfer. *Astrophys. J.*, **750**, 96, https://doi.org/10.1088/0004-637X/750/2/96.

Robinson, T. D., and D. C. Catling, 2012: An analytic radiative-convective model for planetary atmospheres. *Astrophys. J.*, **757**, 104, https://doi.org/10.1088/0004-637X/757/1/104.

Rodgers, C. D., and C. D. Walshaw, 1966: The computation of infrared cooling rate in planetary atmospheres. *Quart. J. Roy. Meteor. Soc.*, **92**, 67–92, https://doi.org/10.1002/QJ.49709239107.

Schneider, S. H., and R. E. Dickinson, 1974: Climate modeling. *Rev. Geophys.*, **12**, 447–493, https://doi.org/10.1029/RG012i003p00447.

Seeley, J. T., N. Jeevanjee, W. Langhans, and D. M. Romps, 2019a: Formation of tropical anvil clouds by slow evaporation. *Geophys. Res. Lett.*, **46**, 492–501, https://doi.org/10.1029/2018GL080747.

——, ——, and D. M. Romps, 2019b: FAT or FiTT: Are anvil clouds or the tropopause temperature-invariant? *Geophys. Res. Lett.*, **46**, 1842–1850, https://doi.org/10.1029/2018GL080096.

Shine, K. P., I. V. Ptashnik, and G. Rädel, 2012: The water vapour continuum: Brief history and recent developments. *Surv. Geophys.*, **33**, 535–555, https://doi.org/10.1007/s10712-011-9170-y.

Singh, M. S., and P. A. O'Gorman, 2015: Increases in moist-convective updraught velocities with warming in radiative-convective equilibrium. *Quart. J. Roy. Meteor. Soc.*, **141**, 2828–2838, https://doi.org/10.1002/QJ.2567.

Stevens, B., H. Brogniez, C. Kiemle, J. L. Lacour, C. Crevoisier, and J. Kiliani, 2017: Structure and dynamical influence of water vapor in the lower tropical troposphere. *Surv. Geophys.*, **38**, 1371–1397, https://doi.org/10.1007/s10712-017-9420-8.

Tan, Z., O. Lachmy, and T. A. Shaw, 2019: The sensitivity of the jet stream response to climate change to radiative assumptions. *J. Adv. Model. Earth Syst.*, **11**, 934–956, https://doi.org/10.1029/2018MS001492.

Thomas, G. E., and K. Stamnes, 2002: *Radiative Transfer in the Atmosphere and Ocean*. Cambridge University Press, 517 pp.

Thompson, D. W. J., S. Bony, and Y. Li, 2017: Thermodynamic constraint on the depth of the global tropospheric circulation. *Proc. Natl. Acad. Sci. USA*, **114**, 8181–8186, https://doi.org/10.1073/pnas.1620493114.

Vallis, G. K., P. Zurita-Gotor, C. Cairns, and J. Kidston, 2015: Response of the large-scale structure of the atmosphere to global warming. *Quart. J. Roy. Meteor. Soc.*, **141**, 1479–1501, https://doi.org/10.1002/QJ.2456.

Wallace, J. M., and P. V. Hobbs, 2006: *Atmospheric Science: An Introductory Survey*. Academic Press, 504 pp.

Weaver, C., and V. Ramanathan, 1995: Deductions from a simple climate model: Factors governing surface temperature and atmospheric thermal structure. *J. Geophys. Res.*, **100**, 11 585–11 591, https://doi.org/10.1029/95JD00770.

Wilson, D. J., and J. Gea-Banacloche, 2012: Simple model to estimate the contribution of atmospheric CO_2 to the Earth's greenhouse effect. *Amer. J. Phys.*, **80**, 306, https://doi.org/10.1119/1.3681188.

Xu, K. M., T. Wong, B. A. Wielicki, L. Parker, B. Lin, Z. A. Eitzen, and M. Branson, 2007: Statistical analyses of satellite cloud object data from CERES. Part II: Tropical convective cloud objects during 1998 El Niño and evidence for supporting the fixed anvil temperature hypothesis. *J. Climate*, **20**, 819–842, https://doi.org/10.1175/JCLI4069.1.

Zhu, X., M. E. Summers, and D. F. Strobel, 1992: Calculation of CO_2 15-μm band atmospheric cooling rates by Curtis matrix interpolation of correlated-k coefficients. *J. Geophys. Res.*, **97**, 12 787–12 797, https://doi.org/10.1029/92JD01311.